A Computational Study of an Aerospace Structural Panel Subjected to High Velocity Flow

By

Scott A. Williams

Thesis

Submitted to the Faculty of the

Graduate School of Vanderbilt University

in partial fulfillment of the requirements

for the degree of

MASTER OF SCIENCE

in

Mechanical Engineering

January 31st, 2020

Nashville, Tennessee

Approved:

Çağlar Oskay, Ph.D.

Haoxiang Luo, Ph.D.

Robert Pitz, Ph.D.

ACKNOWLEDGMENTS

I would like to take a moment to formally acknowledge several people who have contributed to my time at Vanderbilt University and to the completion of this document. First, I would like to thank my labmates and classmates, especially Cole Brubaker, Darren Tinker, and Josh Webb, who have supported and guided me through the challenges of earning my Master of Science degree. Their constant friendship, competitiveness, and sometimes outright ridicule, helped me get to this point.

I would also like to thank my committee members, Dr. Luo and Dr. Pitz, and my committee chair (and advisor), Dr. Oskay. Thank you for taking the time to not only guide me, but provide constructive feedback on my work at Vanderbilt. I could not have completed this without the encouragement and help that you have provided. In addition, I would like to thank Dr. McNamara of Ohio State University for providing the resources and aerodynamic framework for the panel used in this thesis.

Finally, I would like thank my family, but most importantly my wife, Heidi Williams. There were many nights and weekends that we could have spent camping, hiking or on other such adventures, but instead I was coding, writing, or otherwise indisposed. Thank you for never offering a complaint, even if you didn't quite understand why it looked like I was constantly playing with rainbow-colored squares. I know that you sacrificed a lot so that I could finish this achievement, and for that I will always be grateful.

TABLE OF CONTENTS

LIST OF TABLES

LIST OF FIGURES

NOMENCLATURE

A	Johnson-Cook Material Parameter
B	Johnson-Cook Material Parameter
C	Plastic Modulus
$\hat{C}^{\hat{m}}$	Instantaneous Plastic Modulus
C_1	Williams-Landel-Ferry Material Constant
C_2	Williams-Landel-Ferry Material Constant
C_Y	Johnson-Cook Yield Surface
D_{ijkl}	Tensor of Elastic Moduli
E	Elastic Modulus
G	Shear Modulus
$\bar{G}$	Time Independent Shear Modulus
k	Material Parameter
K_e	Ratio of Deviatoric Moduli
K_{me}	Ratio of Deviatoric Moduli for me^{th} Element
$\bar{L}_{ijkl}$	Time Independent Moduli Tensor
$L^{'}_{ijkl}$	Deviatoric Viscoelastic Moduli Tensor
M	Total Yield Surfaces
$\hat{m}$	Active Yield Surface Notation
m	MYSP Yield Surface Notation
m_{jc}	Johnson-Cook Material Parameter
me	Maxwell Element Number
n	Johnson-Cook Material Parameter
Ma	Mach Number
p	Pressure
$\bar{q}$	Hardening Parameter Variable

q	Hardening Parameter
q_a	Dynamic Pressure
q_{ref}	Hardening Parameter Reference Variable
$\bar{S}$	Equivalent Deviatoric Stress
$\bar{S}^m$	Equivalent Deviatoric Stress at m^{th} Element
S_{ij}	Deviatoric Stress
t	Time
$T^\star$	Non-dimensional Temperature
T_0	Reference Temperature
T_{melt}	Material Melting Temperature
U	Velocity
$u_{i,i}$	Divergence of Deformation Field
X	Location
$\dot{\alpha}_{ij}$	Backstress Rate
$\dot{\alpha}_{ij}^{\hat{m}}$	Active Yield Surface Backstress Rate
α^m	Backstress at m^{th} Element
α_{CTE}	Coefficient of Thermal Expansion
α_T	Temperature Shift Factor
α_T	Temperature Shift Factor
Δt	Time Step
δ_{ij}	Kronecker Delta
$\bar{\varepsilon}^{VP}$	Equivalent Viscoplastic Strain
$\dot{\varepsilon}_{kl}^{VP}$	Viscoplastic Strain Rate
ε_{ij}^{E}	Elastic Strain
ε_{ij}^{T}	Thermal Strain
ε_{ij}^{VP}	Viscoplastic Strain
ε_{ij}^{me}	Maxwell Element Strain

ε_{ij}	Strain
γ	Fluidity Parameter
γ_a	Ratio of Specific Heats
$\bar{\mu}^{\hat{m}}$	Equivalent Translation Tensor
$\mu_{ij}^{\hat{m}}$	Translation Tensor
ν	Poisson's Ratio
ω	Displacement
ρ	Density
σ_Y	Yield Stress
σ_{ij}	Stress
τ	Maxwell Time Parameter
ξ_{me}	Maxwell Constant for me^{th} Element

Chapter 1

Introduction

1.1 Background

Responses of aircraft structures under aerodynamic loading have been extensively studied in the computational aerospace community. Now that high-speed aircraft have become an area of interest, the need for modeling the deformation of aerostructures has become increasingly important. Hypersonic and supersonic aircraft experience cyclic loading of their skin panels, which are made out of thin materials, often metallic alloys. Therefore, these structural components are likely to undergo some plastic deformation when excited with high dynamic loads associated with hypersonic flight. Engineering analysis techniques must be developed so that plastic deformation can be incorporated into analysis models.

Engineering analyses of aircraft generally rely on elastic models of the materials, however, plastic models that are employed in studies such as [1, 2, 3] do not adequately address the cyclical loading of the materials. Aerodynamic forces are dynamic and continually change based on the location on the panel as a function of time. The boundary layer, which causes the majority of the aerodynamic forces, is relatively well-known at low speeds, especially below the speed of sound. However, it is not fully understood at supersonic speeds and is extremely hard to predict at hypersonic speeds.

As modern aircraft are breaking the hypersonic speed barrier, it is becoming necessary to understand and model what loads the boundary layer impart on the materials it contacts, helping to define both the economics and the sustainability of the aircraft. To do this analysis, it is important to look at a suitable material for multiple aircraft types. Titanium, while expensive, is a strong material known for its high temperature applications, which makes it applicable for both upper end supersonic and hypersonic flight.

Titanium has been employed on many high-speed systems including the X-15 and the SR-71. It is also utilized in high heat applications of slower aircraft. These applications include where the exhaust hits the air frame, or areas that could see shock impingement. Ti-6242S, the material chosen for this study, is a high temperature titanium alloy, and from experimental data it is known to exhibit a cyclical hysteresis response [4].

In a structural analysis, an aerodynamic model must be employed to approximate the loads experienced during flight. Computational fluid dynamic surrogates, in conjunction with piston theory, is employed to find the aerodynamic loads that the boundary layer applies to the aerostructure. It has been employed by McNamara et al. [5] to analyze high-speed aircraft skin panels in the past, and it gives reasonable approximations for the aerodynamic pressure loads on the surface of the panel.

This thesis employs a new method for calculating the plastic deformation on structures under high velocity aerodynamic loading. The Multi-Yield Surface Plasticity model increases not only the fidelity of the approximations, but also includes the benefit of handling the cyclical nature of boundary layers. In addition, the popular material model Johnson-Cook has been employed as a way to compare Multi-Yield Surface Plasticity to legacy methods. The Johnson-Cook methodology is regularly implemented in plasticity problems to approximate the plastic deformation portion of a stress-strain curve. Multi-Yield Surface Plasticity compares favorably, when correlated with the same experimental data as the Johnson-Cook method.

1.2 Literature Review

Non-linear dynamic simulation of aircraft structures is a relatively new field of study. Linear or purely elastic methods have been favored since the first development of flight. In the last decade, non-linear and dynamic methods have been growing in popularity according Michael Spottswood [6], who also relates that there needs to be more validation and study of these methods. In Spottswood's paper he shows a correlation between deformation and boundary layer conditions. He points out that many titanium aircraft, such as the X-15, SR-71 and YF-12, show real signs of

plastic deformation on their skin panels, as shown in figure 1.1. Computational approaches couple aerodynamic, aerothermal, and structural solutions to solve these complex problem sets.

Figure 1.1: Deformation of the Skin Panels on a YF-12 at Wright-Patterson AFB[1] [6]

Coupled aerodynamic structural problems are made of two major numerical models. The first is the aerodynamic model, which provides the aerodynamic pressure inputs to the finite element code. The second numerical model is the structural model, a component of which is the material model, the focus of this study. The changes in surface roughness and the structural deformation causes oscillations in the boundary layer of the aerodynamic model. This leads to a coupled simulation method utilizing Finite Element Analysis and Computational Fluid Dynamics to solve a given problem [5]. The optimum way to solve these problems is a tightly coupled solution method where each model is solved and provides inputs for the next iteration of the other model. This is an extremely computational expensive way to solve large problem sets, and until recently, was not feasible [7].

McNamara and Culler discuss the importance and relative lack of research in two-way coupling of the deformation and aerodynamic pressure models [7, 8]. An initial step in bringing around

[1]Reprinted from Journal of Sound and Vibration, Vol 443, S. Michael Spottswood, Timothy J. Beberniss, Thomas G. Eason, Ricardo A. Perez, Jeffrey M. Donbar, David A. Ehrhardt, Zachary B. Riley, Exploring the response of a thin, flexible panel to shock-turbulent boundary-layer interactions, Pages 74-89, Copyright 2019, with permission from Elsevier.

these new types of simulations is using computationally quick and reliable material models [7]. The nature of modeling aerodynamic structures also brings about a need for more than just the typical material models. A simplification commonly made for aerodynamic structural models is to assume that the material response is purely elastic. Few studies in the literature incorporate plastic deformation in simulations [3, 6]. Plastic deformations are typically ignored so that simplifications for aerothermal loading can be applied [8].

In conjunction with updated material models, materials with high temperature and high strength characteristics must be employed in those models. Titanium alloys are well-known in the aerospace community and have been flown on many high-speed aircraft including the SR-71, YF-12, and the X-3. One such titanium alloy, Ti-6242S, shows great high-temperature characteristics and is a strong material according to [9]. Hajari and Anoushe [10, 11] state that Ti-6242S is a material that has shown great promise in the aerospace domain and that new computational approaches should be found to model its behavior. It has excellent high strain rate non-linear properties [12, 13], and is the material analyzed in this study. Su [14] shows in his paper that significant plastic deformation can happen in a titanium skin panel exposed to shear loading, and states that a material model to accurately describe plasticity effects needs to be included.

Yan and Oskay provided an alternative model for viscoelastic-viscoplastic behavior in Ti-6242S [4, 15]. This model is employed as a new method of calculating the viscoplastic strain in aerodynamic structures. Multi-Yield Surface Plasticity, or simply MYSP, is based on a method developed by Mroz [4]. Mroz [16] proposed this method due to the lack of plasticity models with the ability to explain work hardening in materials with complex loading histories. He showed that when multiple yield surfaces are implemented, the unique deformation of experimental data under cyclical loading can be accurately captured in computational models [16]. This allows for the model to be applied in cyclical loading situations, such as aerodynamic forces pulsing on an aircraft skin panel.

Yan and Oskay also propose a viscoelastic model for relaxation and creep in Ti-6242S [17]. Relaxation and creep are important for reusable aircraft, and to show how permanent deformation

occurs. This model is employed in the current study. Although this analysis will not show significant effects from relaxation and creep, it is important to represent it for longer duration simulations.

1.3 Goals and Organization

The goal of this study is to verify the application of the Multi-Yield Surface Plasticity model in modeling the cyclical response of a high-speed aircraft skin panel. In order to achieve this goal, this study focuses on a supersonic skin panel representative of a high-speed aircraft. The panel is made of Ti-6242S. To perform the simulations MYSP is incorporated into a finite element code. The load inputs are generated using the piston theory, which approximates the pressure loading on the panel in high-speed flow. The prediction of MYSP is verified by comparing it to classical Johnson-Cook and elastic analyses.

In addition, the aircraft skin panel is analyzed at various temperatures. These temperatures were selected to match the experimental data obtained from Air Force Research Laboratory. The coupled viscoelastic-viscoplastic models Johnson-Cook, and Multi-Yield Surface Plasticity were first calibrated against experimental data. The calibration simulations used finite element analysis (FEA), and were conducted with various loading schemes including tension, relaxation, and cyclical loading of the specimen.

The rest of this paper is laid out into four additional chapters. Chapter 2 focuses on the aerodynamic loading model. It covers how the load inputs are generated for the panel being analyzed. Chapter 3 covers the computational material models and the calibration study. This chapter introduces the Johnson-Cook model, the Multi-Yield Surface Plasticity model, and the Viscoelastic model, and shows the calibration of the models. Chapter 4 is focused on the computational study of the skin panel, including the description of the finite element model of the skin panel, the results from the computational study, and a discussion of those results. Conclusions, and recommendations for future work are discussed in Chapter 5.

Chapter 2

Aerodynamic Model of a Aircraft Skin Panel

2.1 Aerodynamics Background

High-speed aerodynamics is a challenging field as it does not follow many of the normal rules for basic aerodynamics [18]. Hypersonic (traditionally thought to be above Mach 5) and high supersonic speed regimes cause changes in the thermochemistry of the flow. This makes it difficult for traditional computational fluid dynamics solvers to resolve the resulting conditions. Instead, higher order solvers based on Navier-Stokes equations and empirical flow chemistry models must be utilized. These models are popular in the academic community to run unsteady aerodynamic simulations to understand the structural mechanics on hypersonic aircraft.

McNamara et al. [5, 8, 19] uses piston theory when approximating the structural loads of a panel in high-speed flow, due to its simplicity and ability to approximate the cyclical loading. His work with Adam Culler [7, 8] provides the aerodynamic model for this study. The major difference between Culler's work [7, 8] and the current effort is that the panel examined in Culler's work was using a two-dimensional carbon fiber as a material. The analysis described in the current work instead concentrates on a titanium alloy panel that experiences plastic deformation.

Culler and McNamara [8] employ piston theory to calculate the pressure loads on a skin panel from a representative hypersonic vehicle, a representation of which is shown in figure 2.1. The vehicle is envisioned as a hypersonic aircraft that would be reusable. Like the SR-71, the theoretical aircraft in this study has titanium on many of its surfaces.

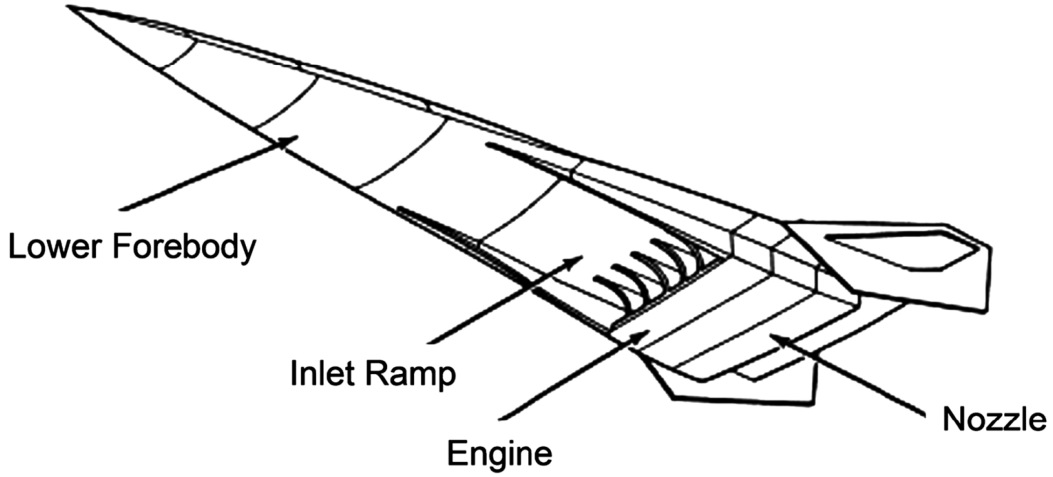

Figure 2.1: Representative Reusable Hypersonic Vehicle[2] [8]

The whole aircraft was not modeled in Culler and McNamara's work [8] due to the computational cost incurred from a simulation of that magnitude. Instead, a single skin panel was modeled. The skin panel is made up of three different bays, each one bounded by a structural stiffener as in figure 2.2.

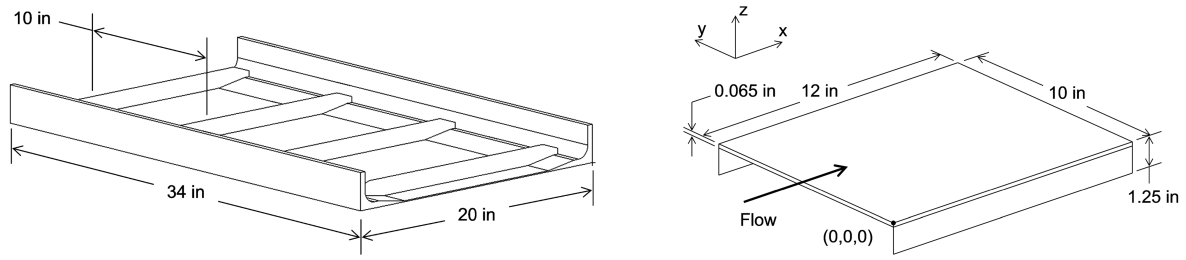

(a) Full Skin Panel

(b) Reduced Skin Panel

Figure 2.2: Representative Skin Panel[2] [8]

To further reduce the computational cost, the model is focused on one of the bays, by considering the periodicity of the panel geometry, similar to [20]. Since the pattern repeats itself, the boundary conditions for each sub panel should be the same and result in similar outputs. This simplified model is shown in figure 2.3, and was also the geometry for the finite element model in

[2]From Impact of Fluid-Thermal-Structural Coupling on Response Prediction of Hypersonic Skin Panels, A. Culler and J. McNamara; reprinted by permission of the American Institute of Aeronautics and Astronautics, Inc.

this study. The panel was modified to fit the goals of this study, which included transitioning the material properties from carbon-carbon to Ti-6242S. In addition, the fidelity of the finite element model was increased to better capture plastic deformation.

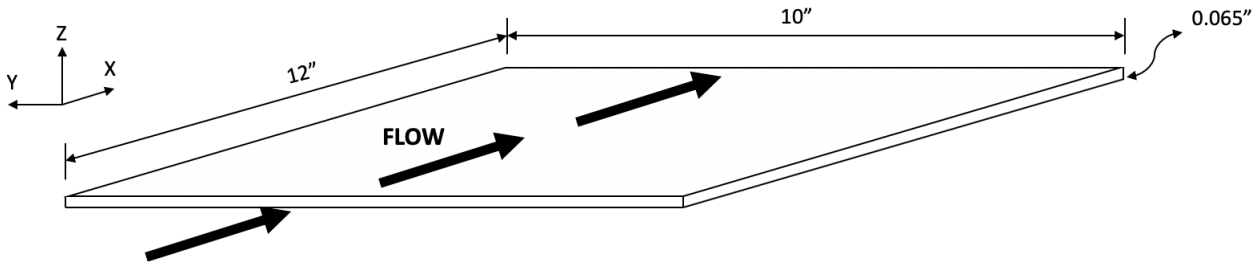

Figure 2.3: Skin Panel Final Geometry

Titanium alloys are generally restricted to applications with peak temperatures less than approximately 560 K [21], but are applicable in non-leading edges and areas that do not see the highest heat fluxes. Even with such restrictions, a large surface area on an aircraft could be made of titanium alloys. The SR-71, which flew to the edge of the hypersonic-supersonic definition line, was made out of titanium. In addition to the SR-71, the X-15, the first rocket powered hypersonic aircraft, utilized titanium on many of its components [22]. The X-15 was limited to Mach 5 in most situations, and its flight trajectory is directly applicable to the speed regime where newer titanium alloys such as Ti-6242S could be applicable.

2.2 Aerodynamic Model

Piston theory is a numerical prediction technique going back to the early 1950s, and was utilized to calculate aerodynamic loads on early hypersonic aircraft. Piston theory is a third order approximation that considers the panel deformation. This allows for an approximation of the flow and an accurate pressure loading during flight [23].

The major difference between piston theory and other aerodynamic loading methods is the approximation of the flow as a piston. The piston reacts to the changes in the surface roughness of the material the flow is passing over, and also takes into account the material deformation [5, 23].

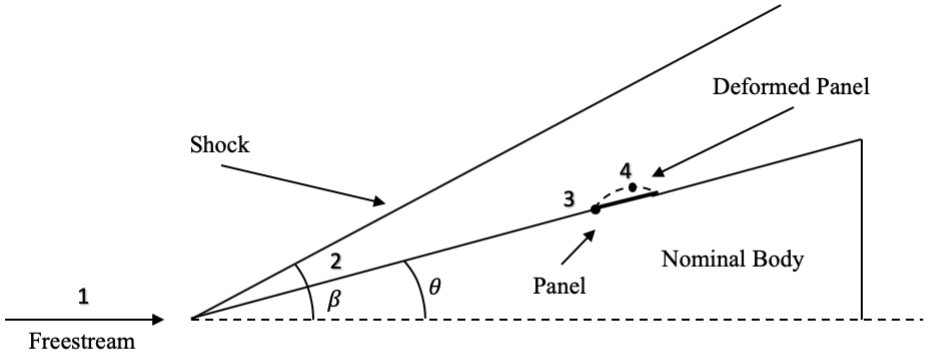

Figure 2.4: Piston Theory Locations with Material Deformation [8]

$$p_4 = p_3 + 2\frac{q_{a3}}{Ma_3}[(\frac{1}{U_3}\frac{\partial \omega}{\partial t} + \frac{\partial \omega}{\partial x}) + \frac{\gamma_a + 1}{4}Ma_3(\frac{1}{U_3}\frac{\partial \omega}{\partial t} + \frac{\partial \omega}{\partial x})^2 + \frac{\gamma_a + 1}{12}{Ma_3}^2(\frac{1}{U_3}\frac{\partial \omega}{\partial t} + \frac{\partial \omega}{\partial x})^3] \tag{2.1}$$

Using figure 2.4 adapted from [8], as a reference, equation 2.1 is used to calculate the pressure at some arbitrary location 4 on the panel. p is the pressure, X is the location, ω is the displacement, Ma is the Mach number, and U is the velocity. Additionally, γ_a is the ratio of specific heats and q_a is the dynamic pressure. The steady state is considered to be the conditions at location 3, this point gives the inputs to the equation. According to [8], the conditions at point 3 are calculated from oblique shock relations, and the displacements for the equation are from the results in [7].

Equation 2.1 can calculate the pressure on the surface of both supersonic and hypersonic aircraft skin panels. It calculates a FEA input based on the location of the element within the domain of the skin panel. Each value will be slightly different due to the unsteady aerodynamics in the

equation [8, 24]. The pressure inputs for the finite element panel in this study were provided by McNamara et al. [3, 7, 8] and were applied separately to the modified panel.

An aerodynamic heating model is also typically applied in a coupled aerostructural problem. An aerodynamic heating model was included in early versions of the elastic test cases for this study, but was removed due to a simplification of the problem. It should be considered for future studies to create a more realistic simulation of high-speed flight.

Chapter 3

Material Models

3.1 Johnson Cook Model

The Johnson-Cook model is commonly used to model the plastic deformation in metallic alloys [25]. The model was developed jointly by Johnson and Cook [26], and has continued to be further refined since its implementation [27]. The model is phenomenological and relies on experimental data to calibrate the material constants for a given material. For the purpose of this analysis, it is included as the reference method to compare against Multi-Yield Surface Plasticity [4, 17].

$$\varepsilon_{ij} = \varepsilon_{ij}^{E} + \varepsilon_{ij}^{VP} + \varepsilon_{ij}^{T} \tag{3.1}$$

$$\varepsilon_{ij}^{T} = \alpha_{CTE}(T - T_0)\delta_{ij} \tag{3.2}$$

As represented in equation 3.1, the total strain ε_{ij} in this model is equal to the combined components of elastic ε_{ij}^{E}, viscoplastic ε_{ij}^{VP}, and thermal strain ε_{ij}^{T}. The thermal strain is defined by equation 3.2. Whereas, α_{CTE} is the coefficient of thermal expansion, and δ_{ij} is the kronecker delta. The stress is expressed by:

$$\sigma_{ij} = D_{ijkl}(\varepsilon_{kl} - \varepsilon_{kl}^{VP}) \tag{3.3}$$

Where σ_{ij} is the stress, and D_{ijkl} is the tensor of elastic moduli. To calculate the viscoplastic strain, the following flow rule is employed.

$$\dot{\varepsilon}_{kl}^{VP} = \gamma \left\langle \frac{f}{C_y} \right\rangle^{q} \frac{\partial f}{\partial \sigma_{ij}} \tag{3.4}$$

The fluidity parameter is γ and the hardening parameter is q [28], which is adjusted with temperature change by:

$$q(T^\star) = q_{ref} + (\bar{q} - q_{ref})T^\star \tag{3.5}$$

The non-dimensional temperature variable $T^\star$ is calculated by:

$$T^\star = \frac{T - T_0}{T_{melt} - T_0} \tag{3.6}$$

Where, T_{melt} is the phase change temperature of the material, T_0 is the reference temperature, and T is the current temperature. The yield function that is employed for this model is the Von-Mises function:

$$f(\sigma_{ij}, C_Y) = \sqrt{3}\bar{S} - C_Y \tag{3.7}$$

The deviatoric stress S_{ij} and equivalent deviatoric stress $\bar{S}$ are calculated using:

$$S_{ij} = \sigma_{ij} - \frac{1}{3}\sigma_{kk}\delta_{ij} \tag{3.8}$$

$$\bar{S} = \sqrt{\frac{1}{2}S_{ij}S_{ij}} \tag{3.9}$$

Where, σ_{kk} is the trace of the stress tensor. The Von Mises yield function requires a yield surface, which in the Johnson-Cook model is expressed as:

$$C_Y = \left[A + B(\bar{\varepsilon}^{vp})^n\right]\left[1 + Cln(\dot{\varepsilon}^\star)\right]\left[1 - (T^\star)^{m_{jc}}\right] \tag{3.10}$$

A, B, m_{jc}, and n are all material parameters, and the equivalent viscoplastic strain $\bar{\varepsilon}^{vp}$ is calculated as:

$$\bar{\varepsilon}^{vp} = \sqrt{\frac{2}{3}\varepsilon_{ij}^{vp} : \varepsilon_{ij}^{vp}} \tag{3.11}$$

As shown in the material model calibration section, while the Johnson-Cook model is widely applied, it is not always the most accurate method. It gives consistent results, but does not include any kind of cyclical model for oscillatory conditions. It is suited for samples that are either placed in tension or compression. The boundary layer in flight causes conditions that not only produce cyclical loads, but vary these loads in location, which will be shown in later calibrations and validations of the models.

3.2 Multi-Yield Surface Plasticity Model

The Multi-Yield Surface Plasticity model, or MYSP, is not a new plasticity model to the material modeling community. It is, however, new to the aerospace structural community. MYSP has a long been used to model soil plasticity [16, 29] but has only been recently transitioned to metals [4]. The primary difference of MYSP is the way plastic flow and material hardening are calculated.

As with the Johnson-Cook viscoplastic model, Multi-Yield Surface Plasticity assumes small strain kinematics. Large plastic deformations [4], which may be seen at high temperatures, are not included in this study. The focus of this study is on oscillatory loading conditions, where loading is large enough to cause plastic deformations.

The strain tensor is made up of three different components as with the Johnson-Cook model, following equation 3.1. MYSP has several key equations in common with the Johnson-Cook method, but the equations must be modified to fit the multi-surface framework. If an arbitrary yield function such as the Von Mises function is taken, σ_Y^m can be expressed as the mth yield surface flow stress. This also makes the function the mth yield surface, and can express each individual yield surface [4, 16]. The modified Von Mises yield function is expressed as:

$$f^m(\sigma,\alpha;\sigma_Y^m) := \sqrt{3}\bar{S}^m(\sigma,\alpha) - \sigma_Y^m \tag{3.12}$$

where, α^m is the backstress and $\bar{S}^m$ is the equivalent deviatoric stress for an arbitrary yield surface. The yield surfaces are a piecewise linear approximation [30] of the plastic portion of the stress strain curve. Adapted from [4] figure 3.1 shows a graphical representation of the yield surfaces.

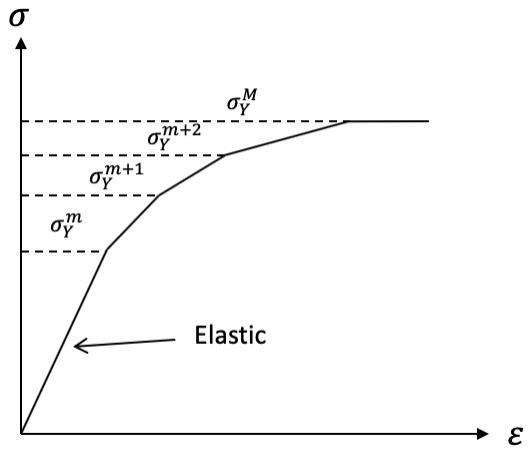

Figure 3.1: Piecewise Linear Approximation Yield Surfaces [4]

The yield surface σ_Y^m is calibrated from the stress-strain response of a given material. The modified equivalent deviatoric stress tensor is calculated using:

$$\bar{S}^m = \sqrt{\frac{1}{2}(S_{ij} - \alpha_{ij}^m)(S_{ij} - \alpha_{ij}^m)} \tag{3.13}$$

A generalization of the Perzyna law specifies the viscoplastic potential [4, 25]. The viscoplastic potential consists of the sum of all contributions from each yield surface as shown in:

$$\Omega(f^1, f^2, ..., f^M) = \sum_{m=1}^{M} \Omega^m(f^m) \tag{3.14}$$

Each surface is modeled using:

$$\Omega^m = \frac{\gamma \sigma_Y^m}{q+1} \left\langle \frac{f^m}{\sigma_Y^m} \right\rangle^{q+1} \tag{3.15}$$

In which γ is the fluidity parameter, and to calculate the hardening variable q equation 3.5 is again employed. When the two equations are combined they become:

$$\dot{\varepsilon}_{ij}^{VP} = \sum_{m=1}^{M} \gamma \left\langle \frac{f^m}{\sigma_Y^m} \right\rangle^q \frac{\partial f^m}{\partial \sigma_{ij}} \tag{3.16}$$

M is the active yield surface, since only active yield surface components are summed to get the viscoplastic strain rate.

$$\frac{\partial f^m}{\partial \sigma_{ij}} = \frac{\sqrt{3}}{2\bar{S}^m}(S_{ij} - \alpha_{ij}^m) \tag{3.17}$$

The backstress is calculated using Prager's model, and uses piecewise linear kinematic hardening [4, 15]. The hardening evolution law for a given yield surface is:

$$\dot{\alpha}_{ij} = C\dot{\varepsilon}_{ij}^{VP} \tag{3.18}$$

Where C is the plastic modulus. For the current active yield surface equation 3.18 becomes:

$$\dot{\alpha}_{ij}^{\hat{m}} = \hat{C}^{\hat{m}} \mu_{ij}^{\hat{m}} \tag{3.19}$$

Each active yield surface will have an instantaneous plastic modulus, which is given by $\hat{C}^{\hat{m}}$. The translation tensor is defined as:

$$\bar{\mu}_{ij}^{\hat{m}} = \frac{\sigma_Y^{\hat{m}+1}}{\sigma_Y^{\hat{m}}}(S_{ij} - \alpha_{ij}^{\hat{m}}) - (S_{ij} - \alpha_{ij}^{\hat{m}+1}) \tag{3.20}$$

The normalized direction of the active yield surface is:

$$\mu_{ij}^{\hat{m}} = \frac{\bar{\mu}_{ij}^{\hat{m}}}{||\bar{\mu}^{\hat{m}}||} \tag{3.21}$$

This was first proposed by Mroz, in 1967 [16]. The instantaneous plastic modulus for the active yield surface can be calculated by:

$$\hat{C}^{\hat{m}} = C^{\hat{m}} \mu_{ij}^{\hat{m}} \dot{\varepsilon}_{ij}^{vp} \tag{3.22}$$

In equation 3.22, $C^{\hat{m}}$ is the plastic modulus of the active yield surface, and the viscoplastic strain rate is the sum for all the yield surfaces up to the active yield surface.

$$\dot{\alpha}_{ij}^{m} = \hat{C}^{\hat{m}} \mu_{ij}^{\hat{m}}; \quad (m \leq \hat{m}) \tag{3.23}$$

Evolution of the backstress for each yield surface is calculated using equation 3.23, where care is taken to satisfy the colinearity condition [4].

The yield surfaces can be calculated using the following expression:

$$\sigma_Y^m(T^\star) = \sigma_Y^1(T^\star) + \frac{(m-1)(\sigma_Y^M - \sigma_Y^1(T^\star))}{M-1} \tag{3.24}$$

In addition, since the MYSP model needs to be used for varying temperature sets, a non-dimensional temperature parameter $T^\star$ must be calculated as shown in equation 3.6. Correlations must be made for the yield stress surfaces $\sigma_Y^m(T^\star)$ and the plastic modulus $C^m(T^\star)$, these can be calculated by:

$$\sigma_Y^m(T^\star) = \sigma_Y^m(T_i^\star) + (\sigma_Y^m(T_j^\star) - \sigma_Y^m(T_i^\star)) \frac{T^\star - T_i^\star}{T_j^\star - T_i^\star} \tag{3.25}$$

$$C^m(T^\star, \sigma_Y^m) = C^m(T_i^\star, \sigma_Y^m) + (C^m(T_j^\star, \sigma_Y^m) - C^m(T_i^\star, \sigma_Y^m)) \frac{T^\star - T_i^\star}{T_j^\star - T_i^\star} \tag{3.26}$$

As with the Johnson-Cook model, the Multi-Yield Surface Plasticity model has its own set of restrictions. It is semi-empirical based, and implementation is limited unless large data sets are available to find the Prager's modulus and the yield surface values. A relatively small data set of five quasi-static tensile tests is available for this study. The tensile experimental data sets include

four different temperatures and two different strain rates (at only one of the temperatures). This is a major shortcoming when trying to determine the empirical parameters and creates uncertainty for this study.

3.3 Viscoelastic Model

Viscoelasticity has also been included in both material models. The viscoelastic model is based on Yan's [28] work in coupled viscoelastic-viscoplastic titanium alloys. The viscoelasticity model is a temporal model using the Boltzmann superposition integral. It assumes small strain deformation kinematics and is fully coupled with the plasticity models used in this study. The total strain becomes:

$$\varepsilon_{ij} = \varepsilon_{ij}^{VE} + \varepsilon_{ij}^{VP} + \varepsilon_{ij}^{T} \tag{3.27}$$

Where, ε_{ij}^{VE} the viscoelastic strain, replaces ε_{ij}^{E} from equation 3.1. The Boltzmann superposition integral is:

$$S_{ij}(t) = \int_0^t L_{ijkl}^{'}(t-\tau)\frac{d\varepsilon_{kl}^{VE}(\tau)}{d\tau}d\tau \tag{3.28}$$

It expresses the constitutive relationship between the viscoelastic strain and the deviatoric stress. $L_{ijkl}^{'}$ is the deviatoric components of the time-dependent viscoelastic moduli. If we assume that $L_{ijkl}^{'}$ is symmetric in this application, the deviatoric component of the time-dependent viscoelastic moduli simplifies [4] using:

$$L_{ijkl}^{'} = L_{klij}^{'} = L_{jikl}^{'} = L_{ijlk}^{'} \tag{3.29}$$

The time-dependent viscoelastic moduli can be expressed using the Prony series:

$$L_{ijkl}^{'}(t) = \big[K_e + \sum_{me=1}^{ME} K_{me} exp\big(-\frac{t}{\xi_{me}}\big)\big]\bar{L}_{ijkl}^{'} \tag{3.30}$$

It is important to note that $\bar{L}'_{ijkl}$ is the time independent deviatoric moduli tensor, and that ME is the number of Maxwell elements for the simulation. The ratio of deviatoric moduli is K_e, and K_{me} and ξ_{me} are the ratio of deviatoric moduli on the me^{th} Maxwell element [17]. The deviatoric component of the elastic moduli in an isotropic solid is expressed by:

$$L'_{ijkl}(t) = 2G(t)\big(\delta_{ik}\delta_{jl} - \frac{1}{3}\delta_{ij}\delta_{kl}\big) \tag{3.31}$$

$G(t)$ is the instantaneous shear modulus [17]. When combining equations 3.30 and 3.31, the result is:

$$S_{ij}(t) = 2\bar{G}K_e\varepsilon^{ve}_{ij}(t) + 2\bar{G}\sum_{me=1}^{ME} K_{me}\varepsilon^{me}_{ij}(t) \tag{3.32}$$

The independent shear modulus is $\bar{G}$ and ε^{me}_{ij} is the Maxwell element strain. Equation 3.32 gives the deviatoric stress tensor where the Maxwell element strain components are expressed by:

$$\varepsilon^{me}_{ij}(t) = \int_0^t exp\big(-\frac{t-\tau}{\xi_{me}}\big)\frac{d\varepsilon^{ve}_{ij}}{d\tau}d\tau \tag{3.33}$$

Where, ξ_{me} is a material constant associated with the Maxwell element.

Because the relaxation behavior is a function of temperature variation, a scheme to adjust the constants must be employed. The Williams-Landel-Ferry equation is:

$$log\alpha_T(T) = \frac{-C_1(T-T_0)}{C_2 + (T-T_0)} \tag{3.34}$$

The temperature shift factor is α_T, and C_1 and C_2 are both material constants. Whereas, T is the temperature of the test specimen [17]. To solve for the final stress in these equations, the pressure is updated via:

$$p(t) = -ku_{i,i}(t) + 3k[\alpha_{CTE}(T(t) - T_0)] \tag{3.35}$$

This takes the stress from deviatoric to apparent stress, where $u_{i,i}$ is the divergence of the deformation field and k is a material parameter.

The above viscoelastic model is applied for both the Johnson-Cook and Multi-Surface Plasticity models. It provides a framework for relaxation of the material. It is calibrated with the plasticity models, and the results are shown in section 3.4.

3.4 Material Model Calibration Studies

The bulk of the experimental test data was provided by Air Force Research Laboratory (AFRL), but some data sets are from literature [4], namely the cyclical loading data sets. The experimental data is used to calibrate and verify each model. All the experimental data is on Ti-6242S and the material properties for the titanium alloy are contained in table 3.1, while the chemical makeup is contained in table 3.2. The model specific parameters for Johnson-Cook [17] and Multi-Yield Surface Plasticity can be found in tables 3.3-3.5, where the number of yield surfaces for MYSP was 11.

Table 3.1: Ti-6242S Material Properties at 296 K

E (GPa)	G (GPa)	ν	σ_Y (MPa)	ρ ($\frac{g}{cc}$)	$\alpha_{CTE}(\frac{\mu m}{m-K})$	γ $\frac{MPa}{hr}$	$\bar{q}$	q_{ref}
114.2	43.25	0.32	990.0	4.54	7.7	2	2.76	1.0

Table 3.2: Ti-6242S Chemical Makeup by Percentage of Weight

Al	Sn	Zr	Mo	Si
6.0%	2.0%	4.0%	2.0%	0.1%

Table 3.3: Johnson-Cook Parameters

A (MPa)	B (MPa)	C	m	n
895.0	125.0	0.0	1.35	0.2

Table 3.4: Multi-Yield Surface Plasticity Plastic Moduli

Plastic Moduli Values by Temperature				
Surface	296.0K (MPa)	811.0K (MPa)	866.0K (MPa)	923.0K (MPa)
1	500,000.0	600,000.0	800,000.0	1,000,000.0
2	400,000.0	500,000.0	600,000.0	800,000.0
3	200,000.0	250,000.0	300,000.0	600,000.0
4	150,000.0	160,000.0	180,000.0	400,000.0
5	30,000.0	40,000.0	60,000.0	80,000.0
6	10,000.0	10,000.0	20,000.0	60,000.0
7	400.0	5,000.0	15,000.0	60,000.0
8	300.0	2,000.0	4,000.0	10,000.0
9	200.0	500.0	1,000.0	2,000.0
10	50.0	10.0	10.0	10.0
11	10.0	10.0	10.0	10.0

Table 3.5: Multi-Yield Surface Plasticity Yield Surfaces

	Yield Stress Values by Temperature			
Surface	296.0K (MPa)	811.0K (MPa)	866.0K (MPa)	923.0K (MPa)
1	895.0	350.0	220.0	100.0
2	909.0	388.0	263.0	144.0
3	923.0	426.0	305.0	189.0
4	937.0	464.0	348.0	234.0
5	951.0	502.0	390.0	279.0
6	965.0	540.0	433.0	323.0
7	979.0	578.0	476.0	368.0
8	993.0	616.0	519.0	413.0
9	1007.0	654.0	562.0	458.0
10	1021.0	692.0	605.0	503.0
11	2000.0	2000.0	2000.0	2000.0

The bulk of the data is quasi static tensile data, which is utilized to calibrate the material models. The experimental data in the case of the MYSP, is also used to find the yield surfaces and Prager's moduli. In addition to the tensile data, there is both data from experiments with cyclical loading and data from relaxation experiments. The relaxation experimental data is important to calibrate the viscoelastic parameters. Table 3.6 shows the tensile experimental test conditions. There are five cases that cover different strain rates and temperatures. All of these cases are loaded in tension, achieved by displacement of the specimen at a constant rate specified in the table.

Table 3.6: Tensile Loading Calibration Case Conditions

Data Set	Type	Strain Rate $(1/s)$	Temperature (K)
1	Tension	1×10^{-2}	296.0
2	Tension	2×10^{-4}	296.0
3	Tension	1×10^{-2}	811.0
4	Tension	1×10^{-2}	866.0
5	Tension	1×10^{-2}	923.0

In figures 3.2 and 3.3 respectively, the Johnson-Cook model and the Multi-Yield Surface Plasticity model tension calibration results are shown. When looking at the plots it can be seen that while the Johnson-Cook model does approximate the stress, the error is appreciable enough to be detected. The Johnson-Cook model particularly appears to have trouble with the higher temperature cases.

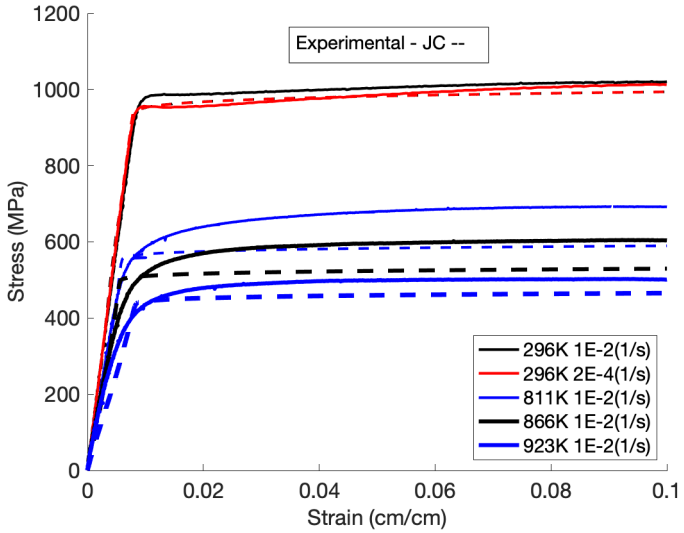

Figure 3.2: Johnson-Cook Model Tensile Calibration Results

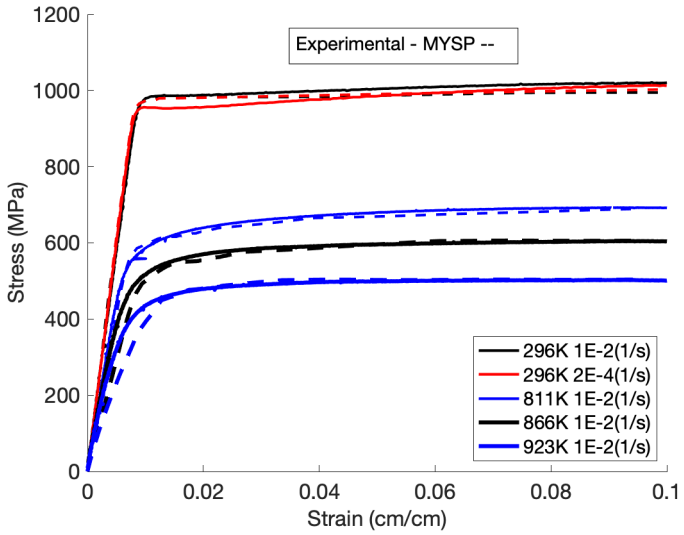

Figure 3.3: Multi-Yield Surface Plasticity Model Tensile Calibration Results

The MYSP calibration plots show that there is generally an increase in accuracy between the model and the experimental data. The one shortcoming is during the initial low strain phase, the MYSP model starts to incur plastic strain, causing a deviation from the elastic experimental data. It appears the simulation is deviating during the elastic phase (the initial linear portion) of the stress strain curve, but in actuality there is a slight plastic deformation during this time.

The relaxation calibrations cover the viscoelastic components of both plasticity models. To experimentally run a relaxation test, the specimen is displaced to a prescribed percent strain and then held at that displacement for a given amount of time. This allows the specimen to relax while still being in a deformed state, and results in the stress reducing to near zero in viscoelastic materials. The calibration test conditions are located in table 3.7, and the calibrated parameters used for the viscoelastic model are in tables 3.8-3.9. Each relaxation case was allowed to run for 100 hours in simulation time after being loaded, the loading of the sample was complete after 18 seconds in simulation time.

Table 3.7: Viscoelastic Calibration Case Conditions

Data Set	Type	Strain Rate $(1/s)$	Temperature (K)
1	Relaxation	1×10^{-2}	866.0
2	Relaxation	1×10^{-2}	923.0

Table 3.8: Viscoelastic Material Constants

ME	K_e	K_1	K_2	K_3	K_4	K_5	C_1	C_2
5	0.0	0.5	0.2	0.15	0.1	0.05	-6.3714	-1094.75

Table 3.9: Viscoelastic Time Parameters

$\xi_1(Hr)$	$\xi_2(Hr)$	$\xi_3(Hr)$	$\xi_4(Hr)$	$\xi_5(Hr)$
4.5e4	4.667e6	4.167e7	4.167e8	4.167e8

Figure 3.4 shows the first forty seconds of the simulations, and the experimental data for both test cases. From the plot, it can be inferred that the model does a better job correlating with the lower temperature test cases. This is also shown in Yan's 2015 work [17] using the same experimental data.

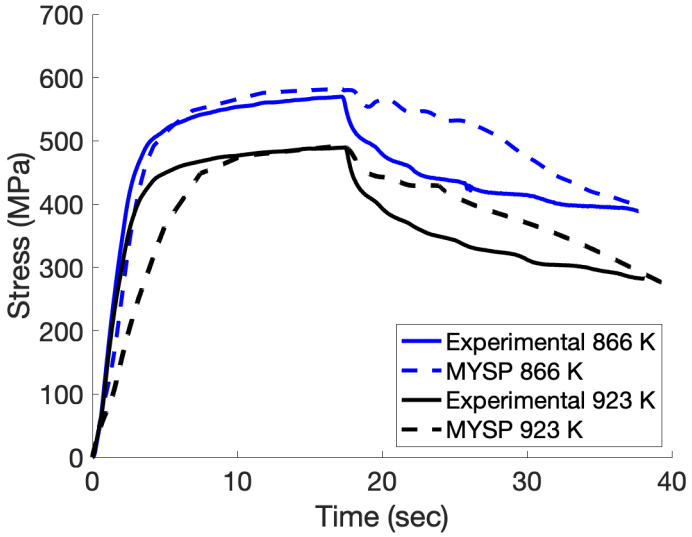

Figure 3.4: Relaxation of Ti-6242S at Two Different Temperatures

The error during the elastic and initial plastic phases are from the plasticity model employed. The stress state is relaxing in the correct general direction, and while initially they do not converge, they do correlate by the end of the forty seconds shown.

At the one hour mark, which is shown in the plots from figure 3.5, it can be seen that both calibration simulations are matching with the experimental data. The lower temperature case ($866K$) does show some variation from the experimental data and is estimated to be approximately 5-10 MPa. This error is within the expected results, and when compared to similar results, looks to be in kind with this model. The ($923K$) case starts with some variation near the 0.2 hour mark, but shows to be matching with the experimental data by the end of the one hour time frame.

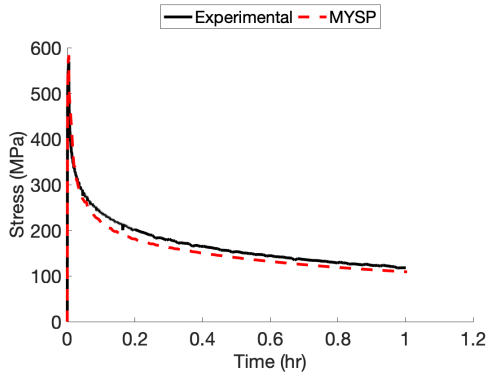

(a) 1 Hour Relaxation at 866K

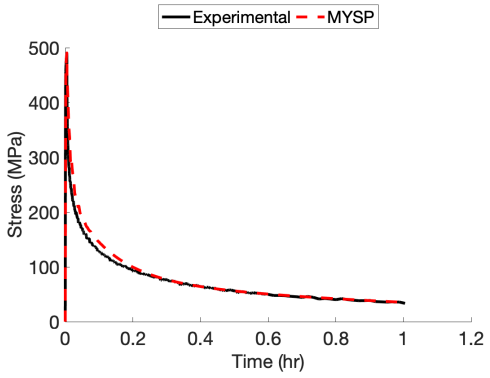

(b) 1 Hour Relaxation at 923K

Figure 3.5: 1 Hour Relaxation Material Model Calibration

It should be noted that some differences between the model and experimental data is expected due to both uncertainty in the experimental data, and model calibration errors. The final relaxation plots shown in figure 3.6 show that at one hundred hours, the difference between the model and the experimental data is small. In plot (b) there appears to be a small amount of numerical error causing the simulation to show an uptick in stress at the 100 hour mark.

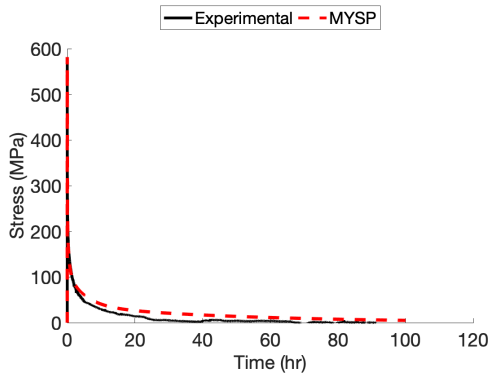

(a) 100 Hour Relaxation at 866K

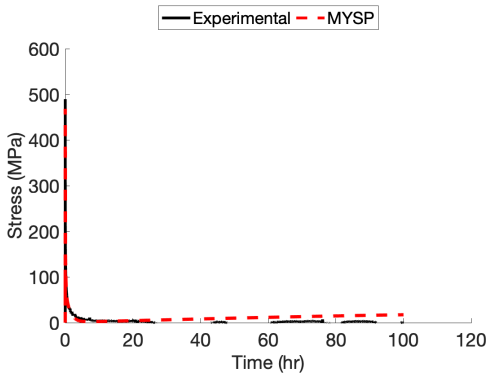

(b) 100 Hour Relaxation at 923K

Figure 3.6: 100 Hour Relaxation Material Model Calibration

The cyclical loading calibration simulations are controlled by displacement. First, the numerical specimens are subjected to tension followed by compression. The tests are uniaxial, with the other two directions deforming due to the Poisson effect. The conditions and strain rates are

contained in table 3.10. Two sets of experimental data are available, and were employed to validate the MYSP model. Additional conditions, including lower temperature experimental data sets, would be preferable to fully validate the cyclical model. Given the limited set of data provided, the following figures show that while the simulations correlate, further data is needed to refine the model.

Table 3.10: Cyclical Loading Calibration Case Conditions

Data Set	Type	Strain Rate $(1/s)$	Temperature (K)
1	Cyclical	1×10^{-2}	723.0
2	Cyclical	1×10^{-2}	823.0

In figure 3.7, the results for the $723K$ data set simulation are shown. The strain and stress history correspond with respect to time, while the stress vs. strain has some error in it.

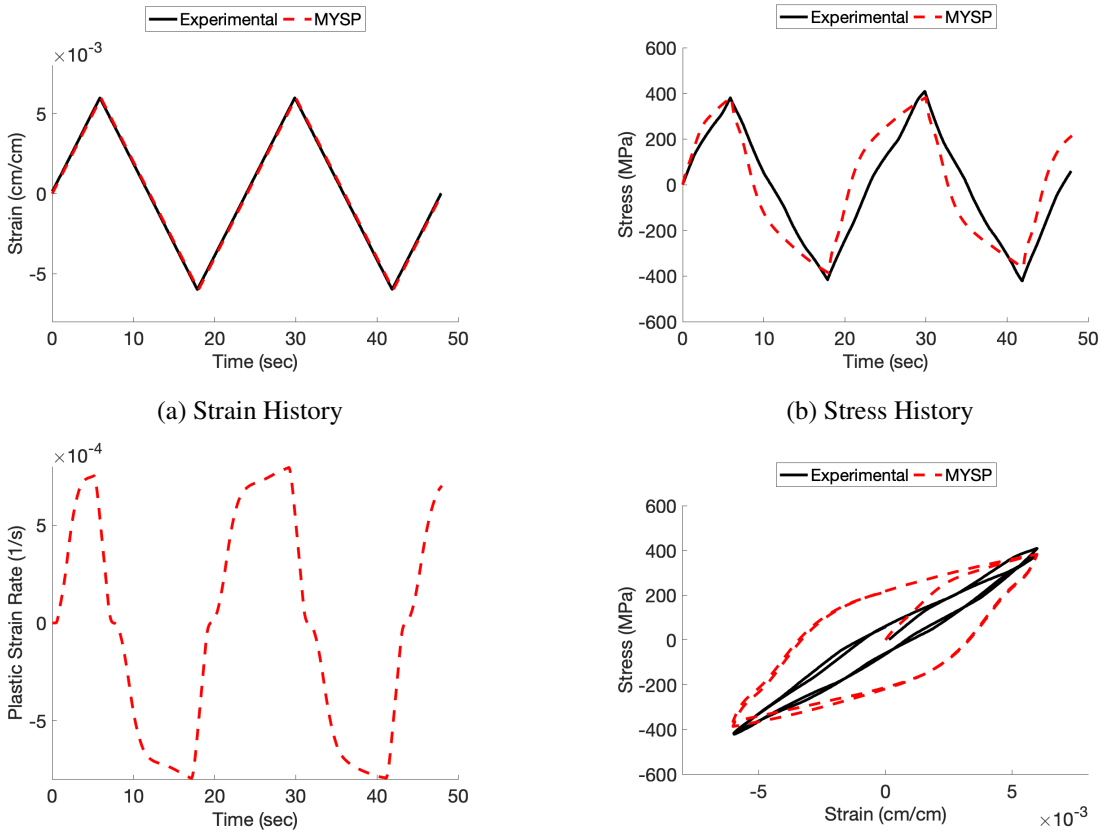

(a) Strain History

(b) Stress History

(c) Plastic Strain

(d) Stress vs. Strain

Figure 3.7: Cyclical Material Model Calibration at 723K

Figure 3.8 shows the 823K test case. It shows an improved correlation between stress and strain when compared to the 723K test case shown in figure 3.7. There are two sources of error that could be contributing to this: the explicit method that was not used in past papers, and the lack of additional data to help calibrate the model. In addition, the experimental data in figure 3.7 and figure 3.8 came from literature [4] as opposed to the Air Force Research Laboratory. Differences in processing, and material characteristics of the Ti-6242S could be contributing to the error between the experimental data and simulation results for the cyclical loading cases.

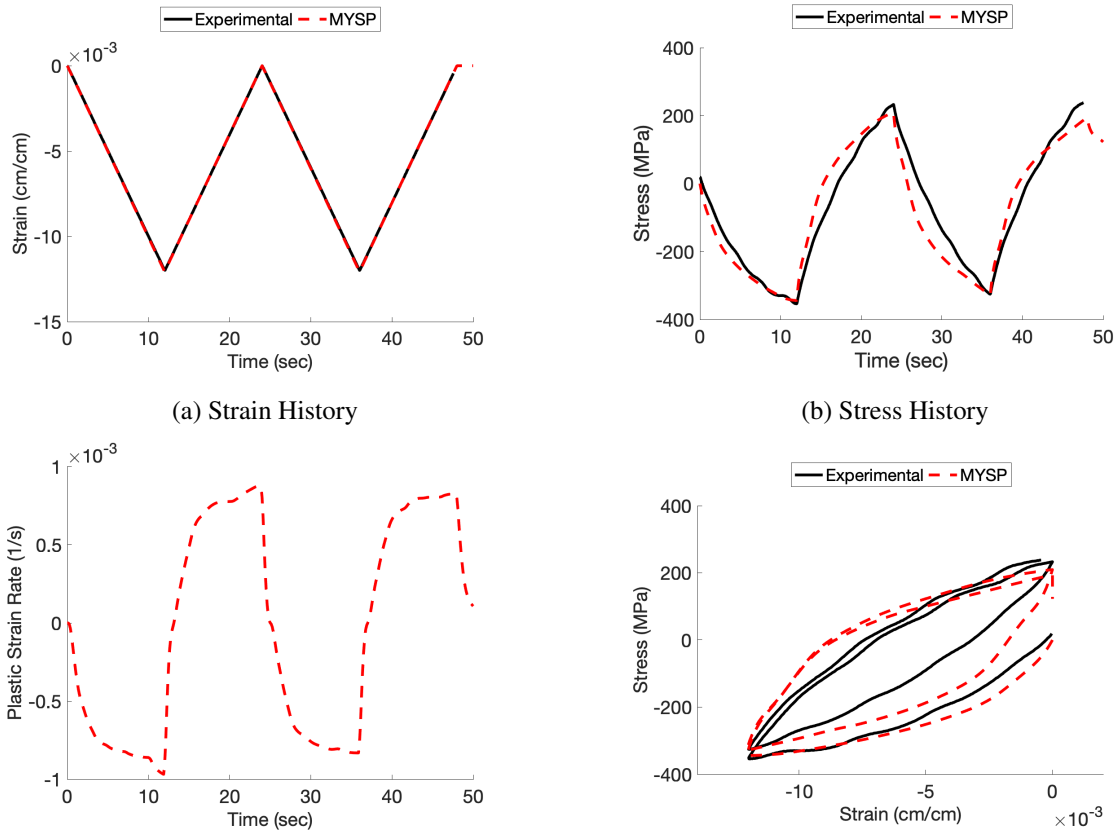

(a) Strain History

(b) Stress History

(c) Plastic Strain

(d) Stress vs. Strain

Figure 3.8: Cyclical Material Model Calibration at 823K

Overall, the calibration results show comparative correlations with the experimental data. The results of the MYSP simulation compared to the tensile experimental data agreed within a small amount of error. Although both the relaxation and cyclical simulations did correlate, the modeling still needs future refining. This can be done by adding extra experimental data sets to the calibration data repository. The main sources of error that contribute to these results are the lack of additional strain rates for both the relaxation test cases and cyclical loading cases. In addition, the lack of temperature variation in the cyclical cases contributes to the error for the MYSP model. To mitigate some of the calibration shortfalls, additional constraints will be placed on the finite element model, such as only using four constant temperatures instead of an aerothermal model in the skin panel simulations.

Chapter 4

Computational Analysis of an Aircraft Skin Panel

4.1 Test Cases, Boundary Conditions, and Applied Loads

As shown in figure 2.2, the representative panel is a single bay of the high-speed aircraft skin panel. The panel is featured in many of Culler and McNamara's works [7, 8], and is a nominal model of a reusable hypersonic aircraft. The panel geometry was input into FEA software, and the explicit analysis capability was used to simulate the panel. Explicit FEM is typically the software of choice for dynamic applications where small time steps are needed. An example of the FEA panel is shown in figure 4.1.

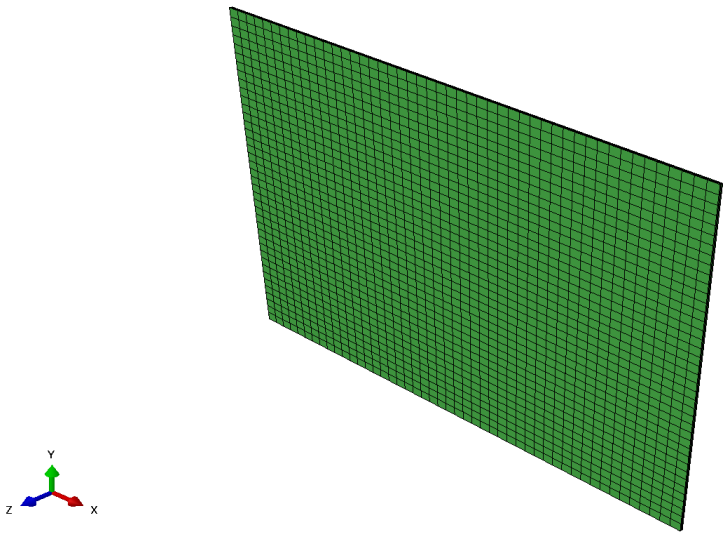

Figure 4.1: 3-D Finite Element Skin Panel Showing Thickness

The panel is made up of 5760 elements, and is three elements thick in the Z direction. The elements are C3D8R quadrilateral bricks, which are suited to this application. As noted in the previous section, the assumption of periodicity is applied to simplify the panel into one bay. This is also used in the boundary conditions to pin the edges of the panel. The displacement boundary

conditions are shown in figure 4.2, boundary conditions include a support on the lower Z face of the edges, and a symmetry condition on all edges of the panel.

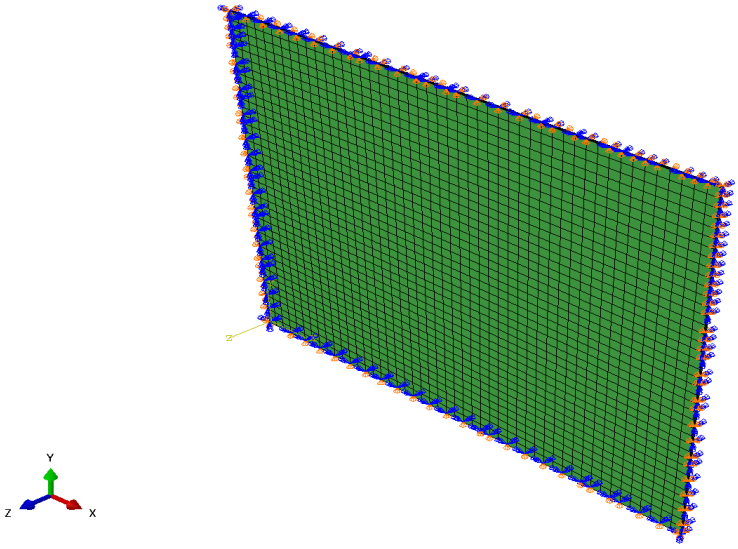

Figure 4.2: 3-D Skin Panel Displacement Boundary Conditions

The loading of the panel is applied only to the face that would be in the high-speed flow. The loading surface is the positive Z directional face, and the flow goes from negative X to positive X, for reference figure 2.2 and 2.3 have the same coordinate system. Each individual surface element receives its own load and amplitude, and these inputs are derived from the aerodynamic model mentioned above. Figure 4.3 shows a representation of how the results for the simulations are displayed.

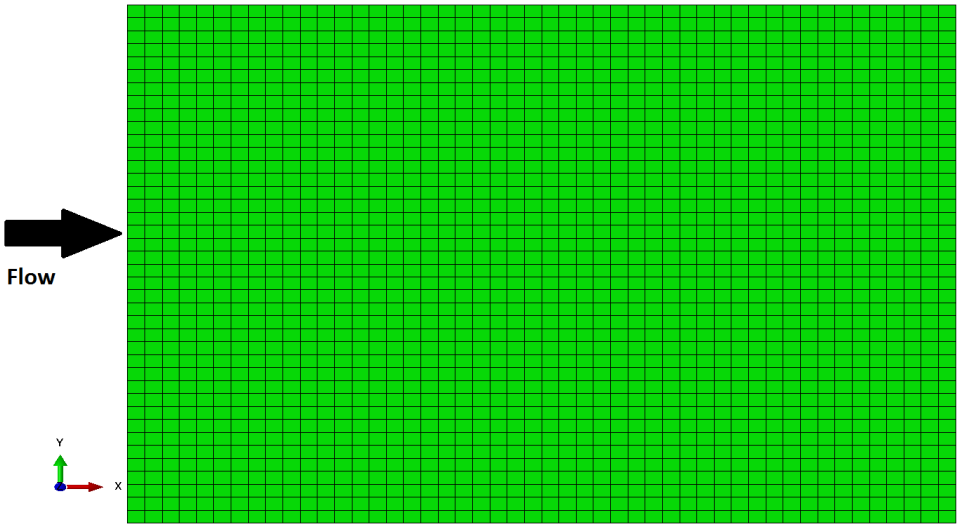

Figure 4.3: 2-D Skin Panel With Flow Direction

The simulation test cases can be found in table 4.1. For this analysis, the temperatures were held constant, this allows for comparisons between the runs, but it also keeps the model close to the material model calibration data. Each test case was used in conjunction with three material models: purely elastic, viscoelastic-viscoplastic using Johnson Cook's model, and viscoelastic-viscoplastic using Multi-Yield Surface Plasticity modeling.

Table 4.1: Aircraft Skin Panel Simulations

Test Case	Mach Number	Altitude (ft)	Temperature (K)
1	Mach 2	20,000	296.0
2	Mach 2	20,000	811.0
3	Mach 2	20,000	866.0
4	Mach 2	20,000	923.0

By using test cases that are standardized, the intent was to make direct comparisons to all three material models. While these cases show a comparison of the models, it is only qualitative in nature, and an exhaustive experimental validation will need to be done in the future. As shown in

the results, these loading conditions do not seem to be sufficient to cause plastic deformation in the finite element model.

As the goal of this study was to compare viscoplastic responses for various models, an additional test case was added to induce plastic strain. An arbitrary test case from table 4.1 was selected for these last three simulations. The additional test case was selected based on temperature, this was to assure that the simulation would get to a plastically deformed state. The greatest chance of plasticity being achieved is at the highest temperature, and test case 4 was selected. To create an increased pressure load, a load multiplier of 5 was applied to the outputs of the aerodynamics model. As seen in section 4.2, plasticity was induced.

4.2 Results

In what follows, we focus the discussion on the high and low temperature responses in the initial test cases. Since viscoplastic behavior is the main focus of this work, the last test case is discussed in more detail.

An important first comparison is that the viscoelastic-viscoplastic model simulation results resemble the purely elastic simulation results, since the simulations did not produce any plastic strain. Figures 4.4-4.5 showcase the $296K$ temperature simulations and show in a qualitative manner that the stress results are not only similar but match within a reasonable amount. Since only the viscoelastic component is being displayed, figure 4.5 represents both the MYSP and Johnson-Cook results. For all figures with the variable $S, Mises$ in the legend, this is the equivalent stress in MPa.

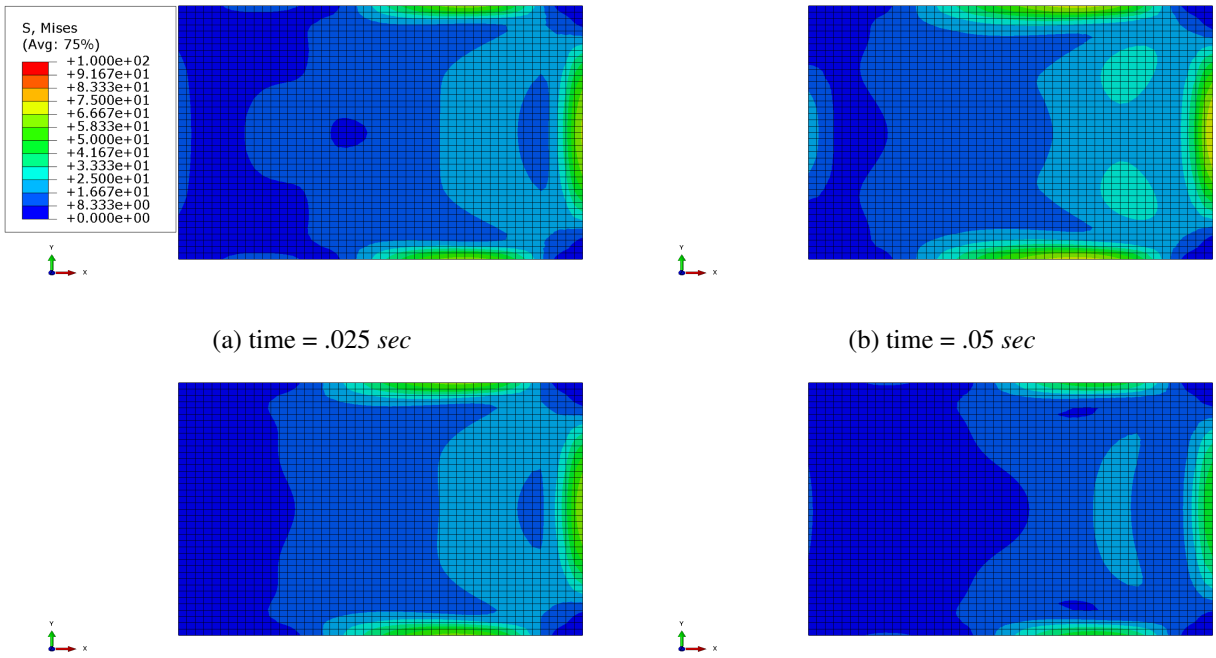

(a) time = .025 *sec*

(b) time = .05 *sec*

(c) time = .075 *sec*

(d) time = .1 *sec*

Figure 4.4: Elastic Stress Results at 296K

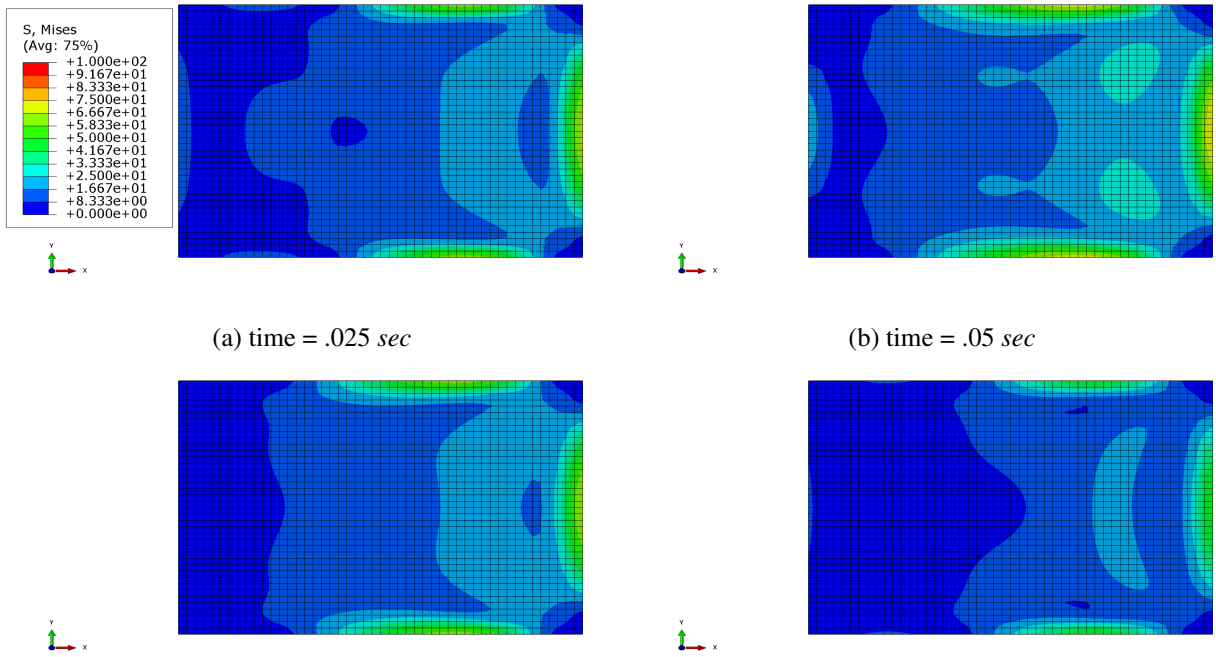

(a) time = .025 *sec*

(b) time = .05 *sec*

(c) time = .075 *sec*

(d) time = .1 *sec*

Figure 4.5: Coupled Viscoelastic-Viscoplastic Stress Results at 296K

While figures 4.6-4.7 show a qualitative comparison, it is important to look at a few select elements and show that the stress, total strain, and viscoplastic strain are in quantitative agreement. To do this, two elements were selected to compare against each other. One element in the center of the panel was selected to show the cyclical nature of the simulations, an element close to the edge in a high stress region was also sampled. The following figures numbered 4.6-4.7 show those comparisons.

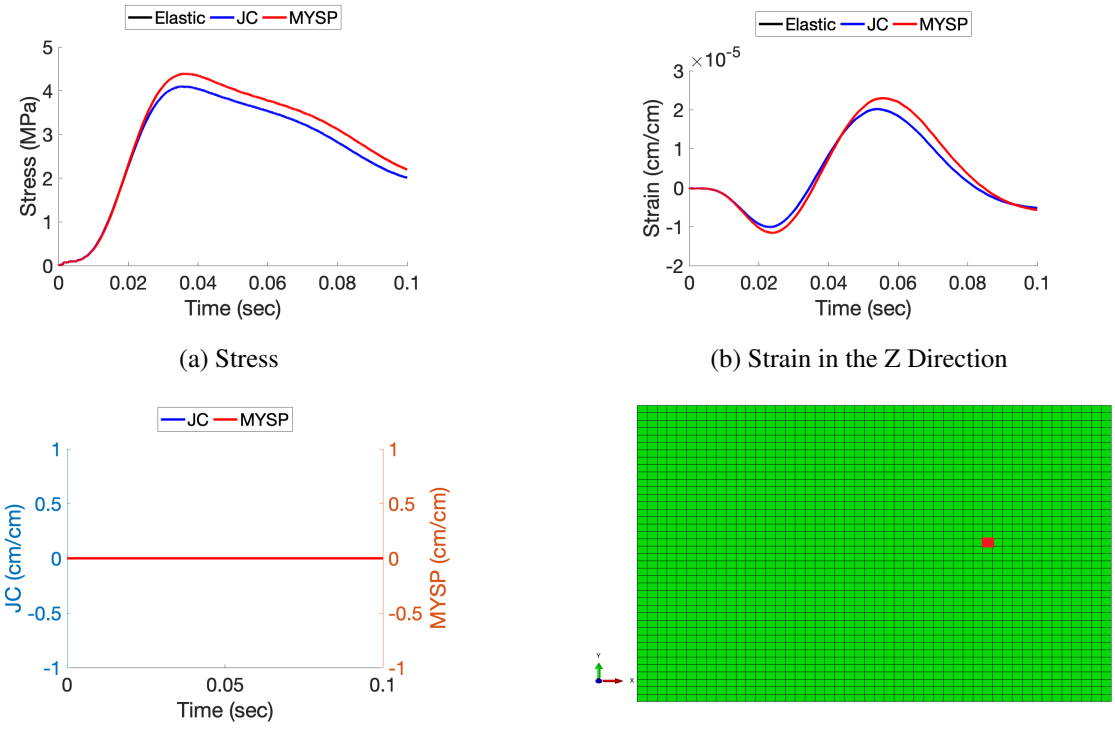

(a) Stress

(b) Strain in the Z Direction

(c) Plastic Strain

(d) Element Location

Figure 4.6: Comparison of Test Case 1 at Element 3085

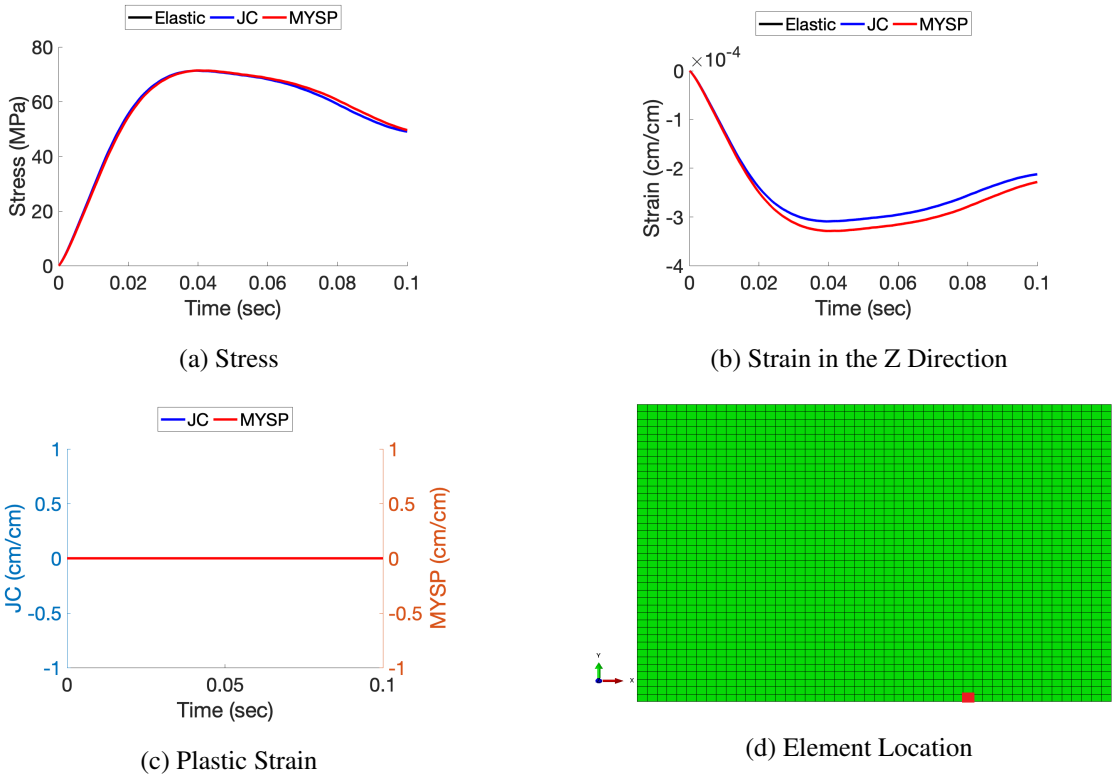

(a) Stress

(b) Strain in the Z Direction

(c) Plastic Strain

(d) Element Location

Figure 4.7: Comparison of Test Case 1 at Element 15

It should be noted in figure 4.6(b) that the strain of the panel is going from negative to positive. It is based on the cyclical loading of the panel from the turbulent boundary layer. This will not show up as much on the edges where the boundary conditions are applied, but it is very apparent at the elements in the middle of the panel.

When test case 4 was run, the qualitative results were similar to test case 1. All results, are in family and keep to the viscoelastic regime for MYSP and Johnson-Cook. Figures 4.8-4.9 show the lack of plastic deformation. As shown in the figures, the panel did not get to a high enough stress state to produce any deformation of the structure. As in earlier figures, for test case 4 figure 4.9 represents both viscoelastic-viscoplastic models since there was no plastic deformation in the simulations.

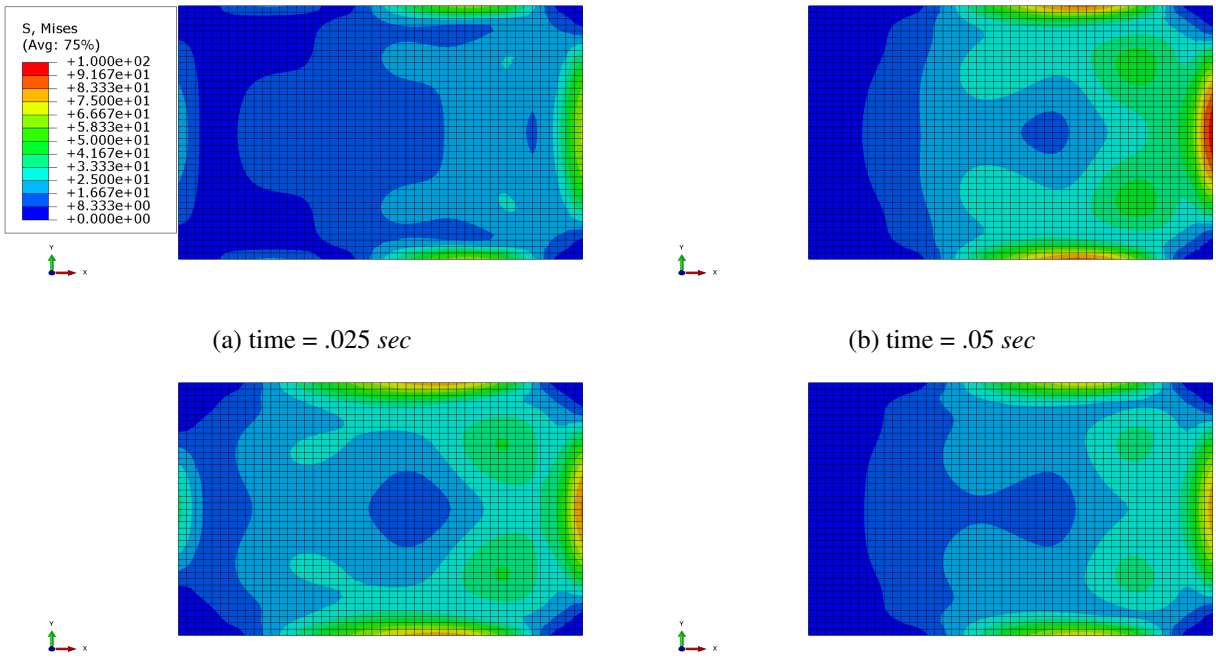

(a) time = .025 *sec*

(b) time = .05 *sec*

(c) time = .075 *sec*

(d) time = .1 *sec*

Figure 4.8: Elastic Stress Results at 923K

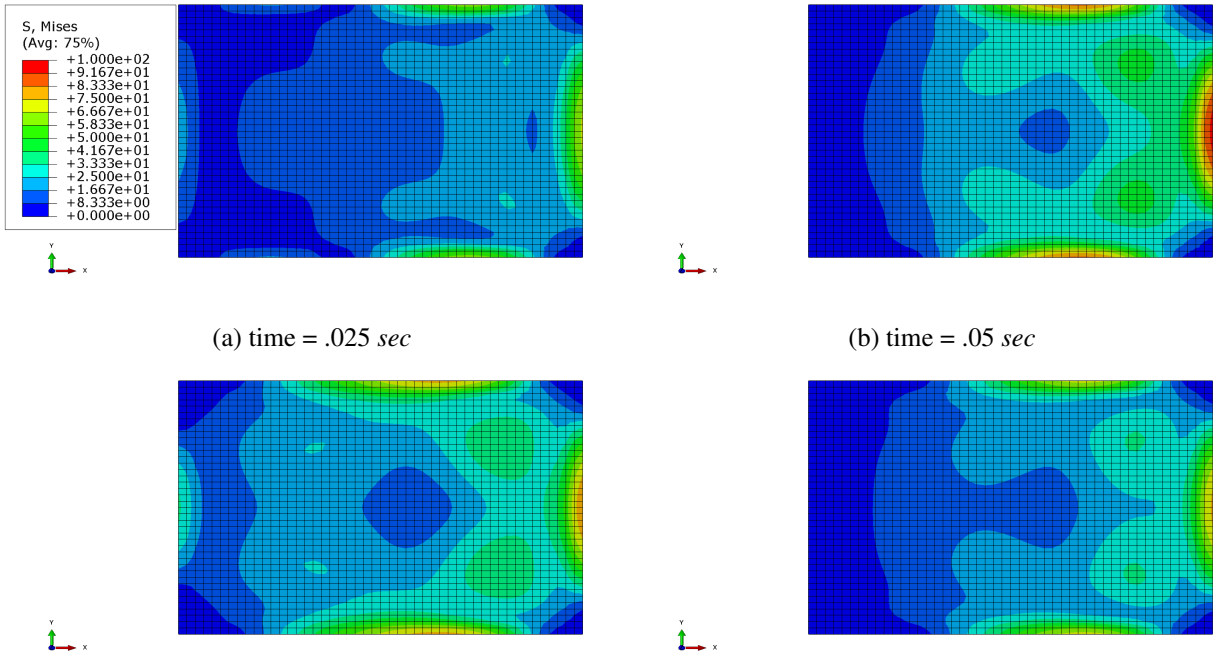

(a) time = .025 *sec*

(b) time = .05 *sec*

(c) time = .075 *sec*

(d) time = .1 *sec*

Figure 4.9: Coupled Viscoelastic-Viscoplastic Stress Results at 923K

To show the quantitative results for test case 4, the same elements as were plotted for test case 1 can be found in figures 4.10-4.11. These show both a center element and edge element as before. It is also apparent, from figures 4.10 and 4.11 that there is no plastic deformation measured on either of the elements. The Multi-Yield Surface Plasticity model did get within 20 MPa of the first yield surface at the 923K temperature, but did not incur any plastic deformation.

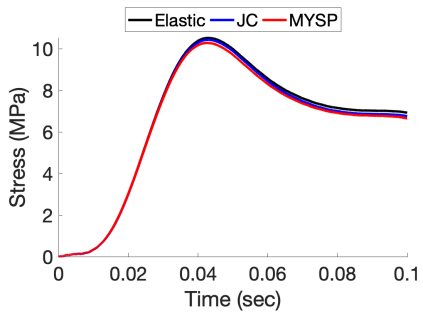

(a) Stress

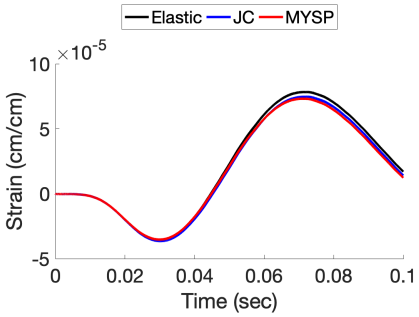

(b) Strain in the Z Direction

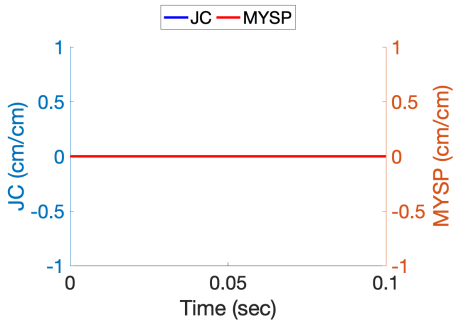

(c) Plastic Strain

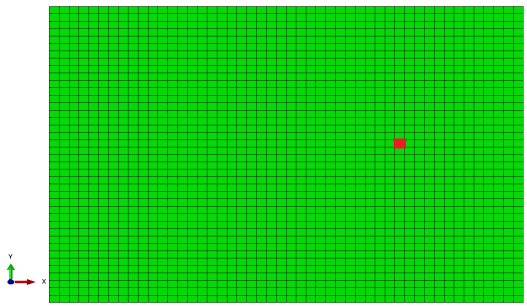

(d) Element Location

Figure 4.10: Comparison of Test Case 4 at Element 3085

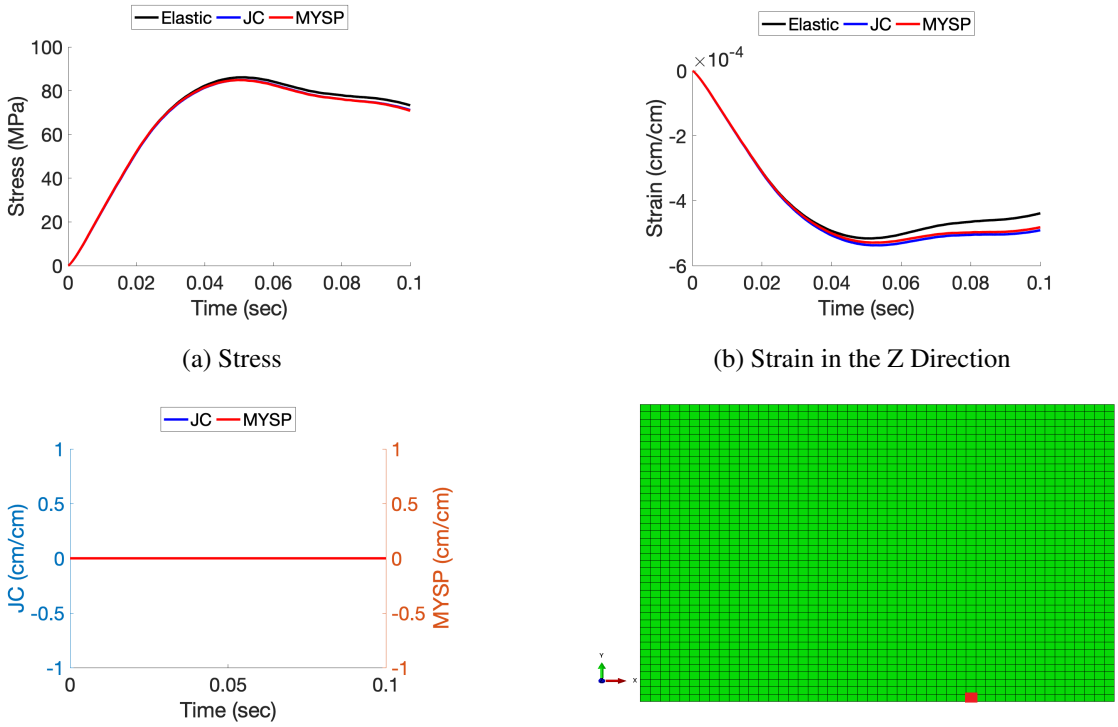

(a) Stress

(b) Strain in the Z Direction

(c) Plastic Strain

(d) Element Location

Figure 4.11: Comparison of Test Case 4 at Element 15

A comparison can be made between the edge elements and the center panel elements from figures 4.10 and 4.11. Although the cyclical loading is greater at the center, because of the boundary conditions near the edges those areas see higher stresses in this analysis. This is especially true of elements that are in the same linear plane as the center of the panel. It occurs in both the X and Y planes of the panel. The high stress state seems to be a result of both being supported in the Z direction from the boundary condition and receiving some of the loading contributions from the less constrained center elements.

It is readily apparent, from the results of both the low and high temperature simulations, that the simulations did not reach the desired plastic deformation state. As discussed in section 4.1, it was decided to implement a loading multiplier to get to the desired stress state and produce plastic strain. To do this, each individual loading curve was multiplied by 5. If there was data at a higher Mach number or lower altitude, these types of loads may have been seen initially but since this

study is limited to Mach 2 for the aerodynamic inputs, this was decided as the best method to achieve plastic results for comparisons.

The amplified loading case produced results displaying plastic deformation in the panel. Figures 4.12, 4.13, and 4.14 all show signs of stress states high enough to cause plastic deformation. The elastic and Johnson-Cook models appear to have similar stress states when compared to the MYSP simulation.

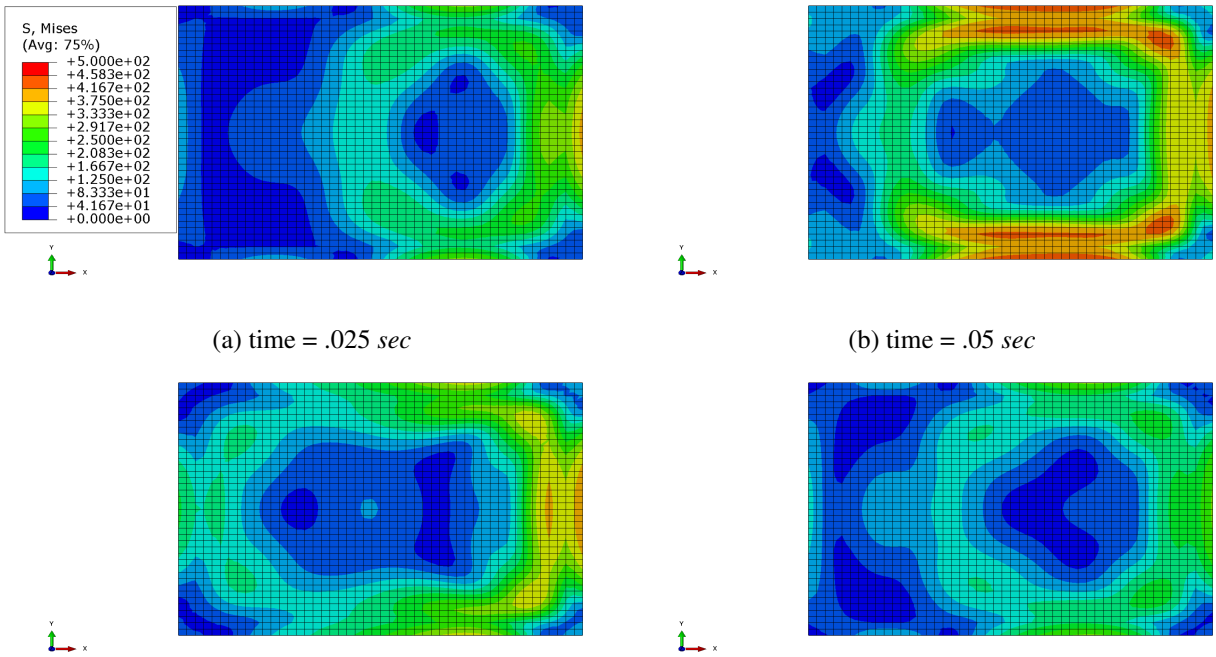

(a) time = .025 *sec*

(b) time = .05 *sec*

(c) time = .075 *sec*

(d) time = .1 *sec*

Figure 4.12: High Amplitude Elastic Panel Stress Results at $923K$

The Johnson-Cook model simulation results shown in figure 4.13 show that the stress was high enough to induce plasticity. Unlike the MYSP simulation, the Johnson-Cook model's yield surface is approximately 500 MPa at this temperature. This translates to a later inducement of plastic strain, keeping the overall stress state a level closer to the elastic simulation.

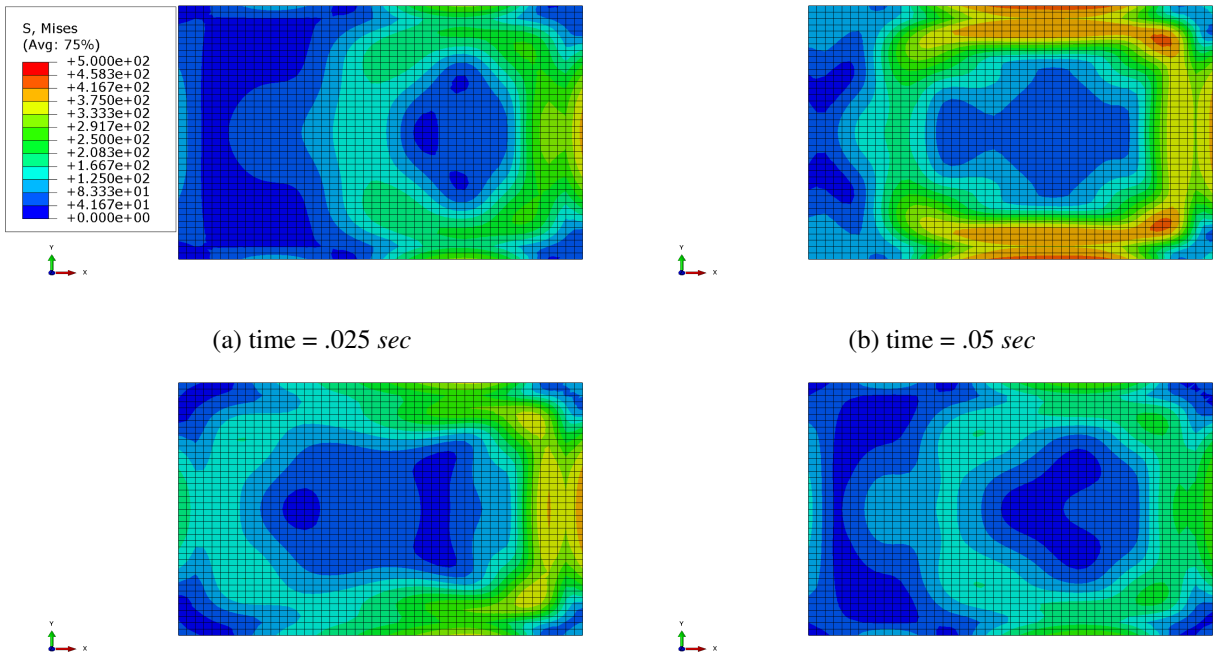

(a) time = .025 *sec*

(b) time = .05 *sec*

(c) time = .075 *sec*

(d) time = .1 *sec*

Figure 4.13: High Amplitude Johnson Cook Panel Stress Results at 923K

The qualitative results from the Multi-Yield Surface Plasticity model simulation in figure 4.14 show a lower stress state than figure 4.12 and figure 4.13. The first yield surface at 923K is 100.0 *MPa* according to table 3.5, and as a result the accumulation of plastic strain started earlier for the MYSP simulation. The overall gradient of the stress field is similar to both the elastic and Johnson-Cook simulations, even though the amplitude is lower than either of those simulations.

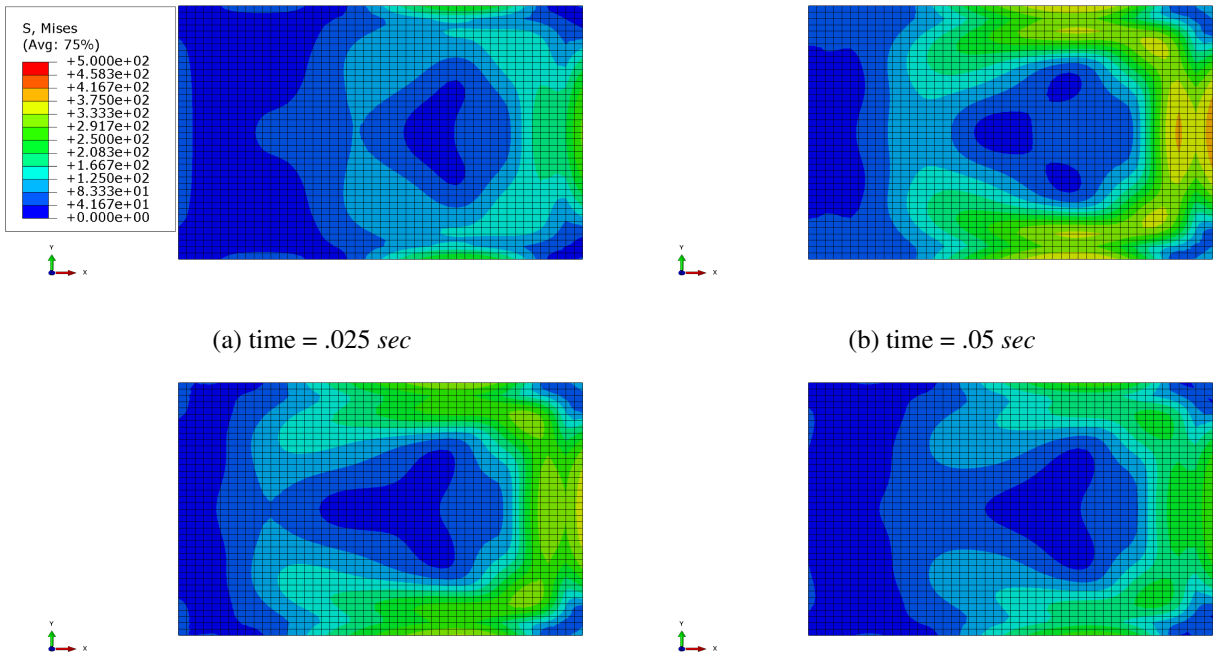

(a) time = .025 *sec*

(b) time = .05 *sec*

(c) time = .075 *sec*

(d) time = .1 *sec*

Figure 4.14: High Amplitude Multi-Yield Surface Plasticity Panel Stress Results at 923K

In figures 4.15 and 4.16, the stress in the Johnson-Cook model response mirrors the elastic simulation response. This matches the qualitative results above, and is another data point showing the late inducement of plasticity in the Johnson-Cook Model. The MYSP model does not follow the Johnson-Cook or elastic simulation results, it shows a lower stress response than either of the other models. While element 3085 did not experience any plastic deformation the strain was decreased as a result of the surrounding plastic deformation in other elements.

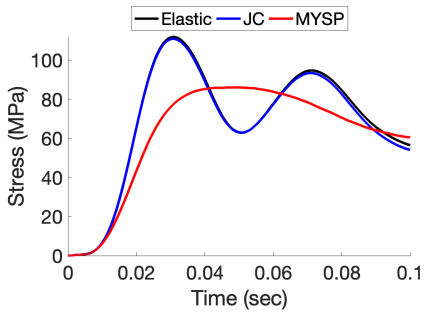

(a) Stress

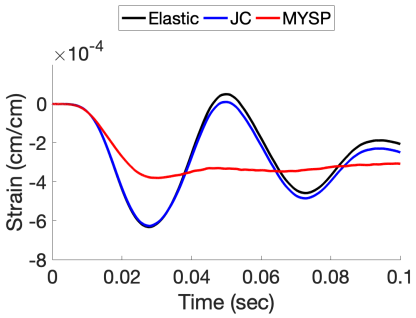

(b) Strain in the Z Direction

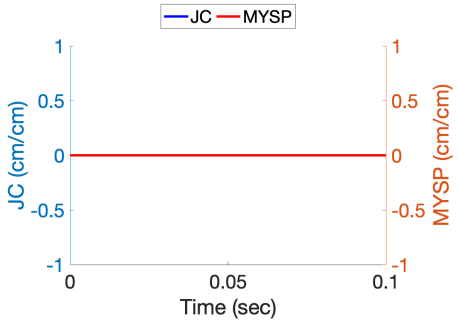

(c) Plastic Strain

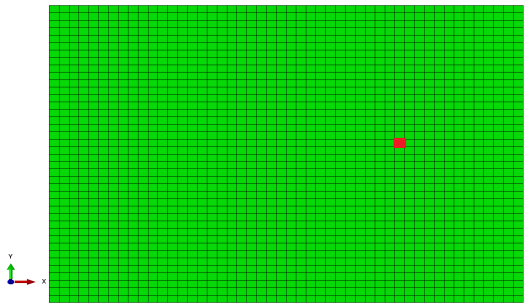

(d) Element Location

Figure 4.15: Element 3085 Comparison Data Plots for High Amplitude Test Case

In contrast to figure 4.15, the stress in figure 4.16 rose to a high enough level that it entered the plastic regime not only for the Multi-Yield Surface Plasticity model but also for the Johnson-Cook model. This can be seen at 0.02-0.04 *sec* mark of the simulation. The MYSP model yields first as expected, and the Johnson-Cook model yields second but does not cross the yield point for a long period of time. The accumulated viscoplastic strain for both the MYSP and Johnson-Cook models is of the same magnitude. The Johnson-Cook viscoplastic strain is half of the MYSP value, and reaches its peak rapidly, while the MYSP model viscoplastic strain accrues over a longer period of time.

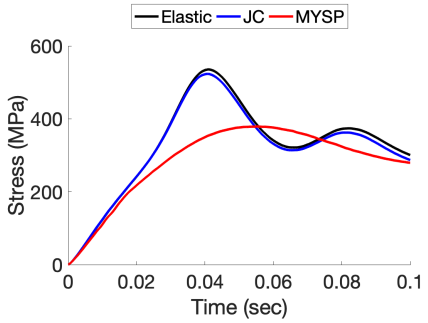

(a) Stress

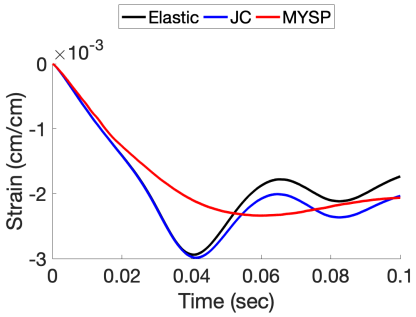

(b) Strain in the Z Direction

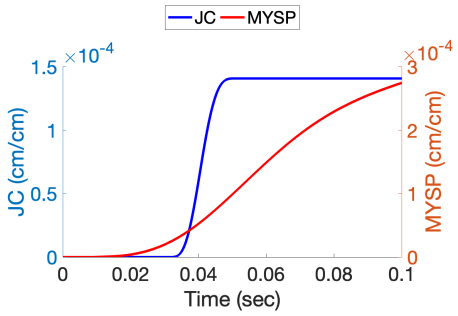

(c) Plastic Strain

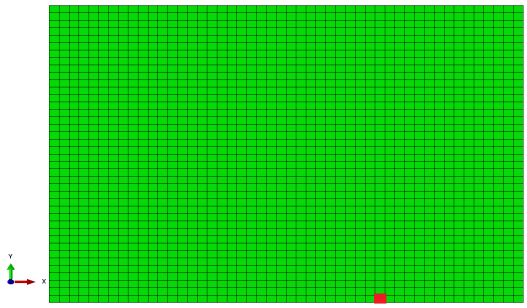

(d) Element Location

Figure 4.16: Element 15 Comparison Data Plots for High Amplitude Test Case

Figure 4.17 and 4.18 show a comparison of the total area affected by viscoplastic strain during the respective simulation. The total area that underwent plastic deformation in the MYSP simulation is larger than the area in the Johnson-Cook simulation. This is an artifact of the difference in yield surfaces between the two coupled viscoelastic-viscoplastic models. Due to the increase of plastically deformed material in the MYSP simulations, the displacement of surrounding elements in those simulations is affected.

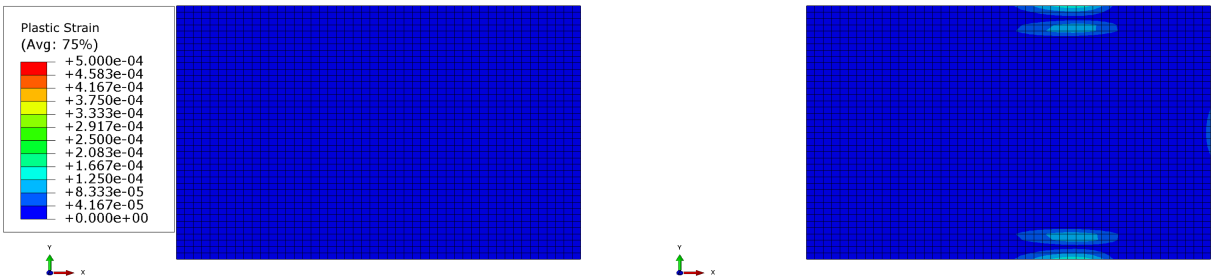

(a) time = .025 *sec*

(b) time = .05 *sec*

(c) time = .075 *sec*

(d) time = .1 *sec*

Figure 4.17: High Amplitude Johnson Cook Panel Plastic Strain Results at 923K

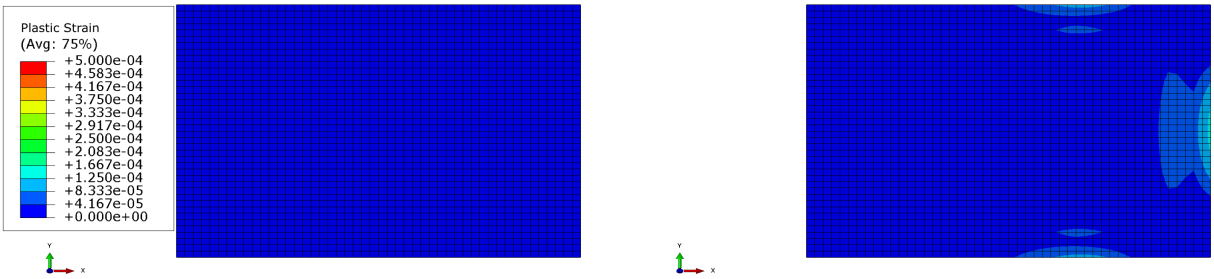

(a) time = .025 *sec*

(b) time = .05 *sec*

(c) time = .075 *sec*

(d) time = .1 *sec*

Figure 4.18: High Amplitude Multi-Yield Surface Plasticity Panel Plastic Strain Results at 923K

The results contained in this section demonstrate several different test cases. Even though the figures were not placed here, test cases 2 and 3 yielded similar results to the other initial test case simulations. They showed results where the stress came close to yielding but was 10-20 MPa below the first yield surface of the Multi-Yield Surface Plasticity method. All test cases matched as shown in figures 4.4-4.11.

4.3 Discussion of Results

The calibration of the material models should be addressed first, before the rest of the study is discussed. This includes the experimental data sets that the models used for calibration, and how the constants applied in the models were derived. For the experimental data sets, all the experiments were at relatively low strain rates, and are be considered to be quasi-static. Strain rates for the panel simulations were considerably higher due to the quickly changing boundary layer from the high-speed flow. The low strain rate of the experimental data hampers the effectiveness of both material models. Since the strain rate of the panel simulations was significantly higher it could lead to error in the viscoplastic strain rate calculated for both models.

Another comparison between the Johnson-Cook and Multi-Yield Surface Plasticity models can be made with respect to the calibration data. If figures 3.2 and 3.3 are compared between the two sets of experimental data, it shows that the MYSP model fits the data with less error. The models tend to correspond through the elastic portion of the experimental data, but diverge as the MYSP simulation starts to cross the early yield surfaces. While those areas do not match as well as the Johnson-Cook simulations, the overall consistency of the MYSP data to the experimental data sets is noticeable. This also translates to the panel simulations, where it shows that more surface area yielded due to the same yield surfaces.

Much of the results section is dedicated to the initial twelve test cases where the results were completely elastic. This is a result of the low loading pressures experienced from the aerodynamic inputs. This also could be a function of the thickness of the panel, and if that thickness is reduced, it could yield results with more plastic deformation. This type of change must happen upfront

before the pressure loading inputs are generated as they will significantly change the aerodynamic outputs.

The simulations that had a load multiplier of 5 showed differences between the Johnson-Cook and the Multi-Yield Surface Plasticity models. The results show that all three material model simulation results have similar stress gradients, with MYSP showing slightly lower stress values due to the plastic deformation. There would be value in comparing the results to a experimental panel put under similar loading to determine which model reflects reality.

The cyclical component of this analysis showed that the Multi-Yield Surface Plasticity model could handle the changes in the oscillatory loading. It did not cause a cessation in the plastic deformation process, though it did change the rate of accumulation. The Johnson-Cook model had a very high viscoplastic strain rate and reached its final state in a short amount of time. This could be an advantage of using MYSP over other methods, and should be studied further.

Chapter 5

Summary, Conclusions, and Future Work

5.1 Summary and Conclusions

In summary, this study shows a new material model for coupled aerodynamic-structural studies. Instead of using traditional techniques for modeling a panel in high-speed flow, Multi-Yield Surface Plasticity is introduced to offer a more versatile approach in describing the viscoplastic behavior of cyclically loaded structures. Cyclical loading is naturally a critical component of the high-speed aerodynamic regime such as supersonic and hypersonic speeds. As such, the MYSP model framework is put forth as a model for these types of simulations.

The Johnson-Cook, Multi-Yield Surface Plasticity, and Viscoelastic models were calibrated using experimental data for various strain rates and temperatures. The calibration experimental data sets include tension, relaxation, and cyclically loaded specimen data for Ti-6242S, a titanium alloy. There are two strain rates available in the experimental data sets, and the temperatures available are either at the reference temperature or the higher end of applicability. Due to the semi-empirical nature of both the Multi-Yield Surface Plasticity model and the Johnson-Cook model some fidelity was lost due to the limited experimental data sets.

The finite element panel analysis compared the Multi-Yield Surface Plasticity model to the Johnson-Cook model as a reference. A high-speed aircraft skin panel made of Ti-6242S was modeled using finite element analysis (FEA) software. To generate the inputs, an aerodynamic model known as piston theory was used in conjunction with a surrogate panel to create cyclical pressure inputs. Piston theory is known for it's ability to create realistic cyclical pressure loading on a skin panel. The aerodynamic model results provided by McNamara et al.[3, 7, 8] were employed as pressure inputs to the finite element analysis software, and the material models were applied to solve for stress, strain, and plastic strain. The results are displayed in figures 4.4 - 4.11 and it was discovered that the initial flight conditions of 20,000 ft at Mach 2 were not sufficient to create

plastic deformation. To induce plastic deformation a multiplier of 5 was used on the pressure input data. This caused the desired effect, and plastic strain was apparent in the results shown in figures 4.12 - 4.16.

The Multi-Yield Surface Plasticity model appears to show favorable results for coupled unsteady aerodynamic-structural problems, a principal conclusion for this study. Beyond this study there needs to be additional studies with an aerothermal model added, to confirm this conclusion. Another conclusion is that there is not currently enough high strain rate and diverse temperature data to fully validate the MYSP framework. Care should be taken to add additional empirical data to derive material constants such as yield surfaces, and the Prager Moduli for MYSP.

This study shows that the utilization of Multi-Yield Surface Plasticity is a reasonable option for computational modeling of high-speed coupled aerodynamic-structural problems. Additional studies need to be undertaken to fully understand the responses in a dynamic temperature environment and under long duration flight simulations. The MYSP model promises to bring additional knowledge to the problem set, when fully validated and tested.

5.2 Future Work

Several key improvements can be made, not only to this study, but also to the Multi-Yield Surface Plasticity model. There were several shortcomings that can be attributed to lack of experimental data, type of data provided, or diversity of the data. The experimental data is important because without it there is no method to calibrate or adjust the material model parameters.

To increase the effectiveness of the Multi-Yield Surface Plasticity model, it would be worthwhile to collect additional quasi-static and high strain rate data at various temperatures. If additional data could be obtained, an improved correlation for the yield surfaces dependencies on temperature could be derived. Currently, this process is a interpolation between the four known data points. The subject experimental data set does not allow for predictions on how strain rate affects changes to the yield surface values. These two suggestions could help significantly in creating an refined predictive model.

The skin panel study was hampered by lack of input data due to it only being a Mach 2 flow field. Additional studies in the future should focus on flight regimes that are more representative of high-speed supersonic or hypersonic flight. As the velocity of the flow field is increased, it is postulated that the boundary layer will become more turbulent, and this will result in larger pressure input loads to the panel.

The last suggestion for future work is to study additional locations of the panel. This panel was located on the underside of the aircraft and may not have been in an area that receives the higher amplitude aerodynamic loads. If a different location were used, the flight conditions of Mach 2 and 20,000 ft could be more relevant for this work. A study should be done on what dependencies the location of the panel has on the aerodynamic loads the panel receives.

BIBLIOGRAPHY

[1] J.T. Oden. Analysis of flow-, thermal-, and structural-interaction of hypersonic structures subjected to severe aerodynamic analysis of flow, thermal, and structural interaction of hypersonic structures subjected to severe aerodynamic heating. Technical Report AFOSR-TR-90-0050, AFOSR, 1990.

[2] James C. Sobotka, Alpay Oral, and Adam J. Culler. Towards a coupled loads-response-life prediction framework for hypersonic structures in combined extreme environments. *54th AIAA/ASME/ASCE/AHS/ASC Structures, Structural Dynamics, and Materials Conference*, 2013.

[3] Jonathen H. LaFontaine, Abhijit Gogulapati, and Jack J. McNamara. Effects of strain hardening on response of skin panels in hypersonic flow. *AIAA Journal*, 54(6):1974–1986, 2016.

[4] Hao Yan and Caglar Oskay. Multi-yield surface modeling of viscoplastic materials. *International Journal for Multiscale Computational Engineering*, 15(2):121–142, 2017.

[5] P.P. Friedmann, J.J. McNamara, B.J. Thuruthimattam, and I. Nydick. Aeroelastic analysis of hypersonic vehicles. *Journal of Fluids and Structures*, 19(5):681 – 712, 2004. Aeroelasticity.

[6] S. Michael Spottswood, Timothy J. Beberniss, Thomas G. Eason, Ricardo A. Perez, Jeffrey M. Donbar, David A. Ehrhardt, and Zachary B. Riley. Exploring the response of a thin, flexible panel to shock-turbulent boundary-layer interactions. *Journal of Sound and Vibration*, 443:74 – 89, 2019.

[7] Adam J. Culler and Jack J. McNamara. Studies on fluid–thermal–structural coupling for aerothermoelasticity in hypersonic flow. *AIAA Journal*, 48(8):1721–1738, 2010.

[8] Adam J. Culler and Jack J. McNamara. Impact of fluid-thermal-structural coupling on response prediction of hypersonic skin panels. *AIAA Journal*, 49(11):2393–2406, 2011.

[9] William D Brewer, R.Keith Bird, and Terryl A Wallace. Titanium alloys and processing for high speed aircraft. *Materials Science and Engineering: A*, 243(1):299 – 304, 1998.

[10] Alireza Hajari, Maryam Morakabati, Seyed Mahdi Abbasi, and Hasan Badri. Constitutive modeling for high-temperature flow behavior of ti-6242s alloy. *Materials Science and Engineering: A*, 681:103 – 113, 2017.

[11] A.S. Anoushe, A. Zarei-Hanzaki, H.R. Abedi, A. Barabi, C. Huang, and F. Berto. On the microstructure evolution during isothermal low cycle fatigue of beta-annealed ti-6242s titanium alloy: Internal damage mechanism, substructure development and early globularization. *International Journal of Fatigue*, 116:592 – 601, 2018.

[12] A.E. Buzyurkin, I.L. Gladky, and E.I. Kraus. Determination and verification of johnson–cook model parameters at high-speed deformation of titanium alloys. *Aerospace Science and Technology*, 45:121 – 127, 2015.

[13] Paramjit Singh, Harish Pungotra, and Nirmal S. Kalsi. On the characteristics of titanium alloys for the aircraft applications. *Materials Today: Proceedings*, 4(8):8971 – 8982, 2017. International Conference on Advancements in Aeromechanical Materials for Manufacturing (ICAAMM-2016): Organized by MLR Institute of Technology, Hyderabad, Telangana, India.

[14] Yuru SU, Zhidong GUAN, Xin WANG, Zengshan LI, Jun GUO, and Yongjie HUANG. Buckling and post-buckling behavior of titanium alloy stiffened panels under shear load. *Chinese Journal of Aeronautics*, 32(3):619 – 626, 2019.

[15] J.L. Chaboche. A review of some plasticity and viscoplasticity constitutive theories. *International Journal of Plasticity*, 24(10):1642 – 1693, 2008. Special Issue in Honor of Jean-Louis Chaboche.

[16] Z. Mróz. On the description of anisotropic workhardening. *Journal of the Mechanics and Physics of Solids*, 15(3):163 – 175, 1967.

[17] Hao Yan and Caglar Oskay. A viscoelastic-viscoplastic model of titanium structures subjected to thermo-chemo-mechanical environment. *International Journal of Solids and Structures*, 56-57:29 – 42, 2015.

[18] Wallace D. Hayes. On hypersonic similitude. *Quarterly of Applied Mathematics*, 5(1):105,106, 1947-04-01.

[19] HOLT ASHLEY and GARABED ZARTARIAN. Piston theory-a new aerodynamic tool for the aeroelastician. *Journal of the Aeronautical Sciences*, 23(12):1109–1118, 1956.

[20] M.C. Simmons and G.K. Schleyer. Pulse pressure loading of aircraft structural panels. *Thin-Walled Structures*, 44(5):496 – 506, 2006.

[21] M. Peters, J. Kumpfert, C.H. Ward, and C. Leyens. Titanium alloys for aerospace applications. *Advanced Engineering Materials*, 5(6):419–427, 2003.

[22] Dennis R Jenkins. *Hypersonics before the shuttle: a concise history of the X-15 research airplane*. National Aeronautics and Space Administration, NASA Office of Policy and Plans, NASA History Office, NASA Headquarters, 2000.

[23] M. J. Lighthill. Oscillating airfoils at high Mach number. *Journal of the Aeronautical Sciences*, 20(6):402–406, 1953.

[24] Chuh Mei, K. Abdel-Motagaly, and R. Chen. Review of Nonlinear Panel Flutter at Supersonic and Hypersonic Speeds. *Applied Mechanics Reviews*, 52(10):321–332, 10 1999.

[25] J.L. Chaboche. Constitutive equations for cyclic plasticity and cyclic viscoplasticity. *International Journal of Plasticity*, 5(3):247 – 302, 1989.

[26] Gordon R Johnson and William H Cook. Fracture characteristics of three metals subjected to various strains, strain rates, temperatures and pressures. *Engineering Fracture Mechanics*, 21(1):31–48, 1985.

[27] Caglar Oskay and Mark Haney. Computational modeling of titanium structures subjected to thermo-chemo-mechanical environment. *International Journal of Solids and Structures*, 47(24):3341 – 3351, 2010.

[28] Hao Yan and Caglar Oskay. A three-field (displacement–pressure–concentration) formulation for coupled transport–deformation problems. *Finite Elements in Analysis and Design*, 90:20 – 30, 2014.

[29] Quan Gu, Joel P. Conte, Ahmed Elgamal, and Zhaohui Yang. Finite element response sensitivity analysis of multi-yield-surface j2 plasticity model by direct differentiation method. *Computer Methods in Applied Mechanics and Engineering*, 198(30):2272 – 2285, 2009.

[30] P.G. Hodge. A general theory of piecewise linear plasticity based on maximum shear. *Journal of the Mechanics and Physics of Solids*, 5(4):242 – 260, 1957.